1

Shallow water anoxia in the Mesoproterozoic ocean: Evidence from the Bashkir Meganticlinorium, Southern Urals

5

6 Katherine A. Doyle[1][*], Simon W. Poulton[1], Robert J. Newton[1], Victor N.
7 Podkovyrov[2] and Andrey Bekker[3]

8

9 [1]School of Earth and Environment, University of Leeds, Leeds, LS2 9JT, UK

10 [2]Institute of Precambrian Geology and Geochronology, Russian Academy of Sciences, St.
11 Petersburg 199034, Russia

12 [3]Department of Earth Sciences, University of California Riverside, CA 92521, USA

13

14

15

16

17

18

19

20

21

22

23

24

25 *Corresponding author: eekd@leeds.ac.uk

33

34   ABSTRACT

35   The apparent lag between the first permanent rise of atmospheric oxygen to appreciable

36   levels and oxygenation of the deep ocean has focused efforts in deciphering the evolution of

37   seawater chemistry across the Proterozoic Eon (2.5–0.542 Ga). It is generally accepted that

38   from ~1.85 Ga oxic shallow marine waters were widespread while the deep ocean remained

39   dominantly ferruginous (Fe(II)-rich), with episodic euxinia confined to productive continental

40   margins and intracontinental basins. The geochemical record that informs this picture,

41   however, is currently sparse, and further studies are required to adequately evaluate temporal

42   and spatial variability in ocean redox conditions across this vast expanse of time. Here, we

43   report Fe-S-C systematics, alongside major (Al, Mn) and trace metal (Mo, U) data for ~1.6–

44   0.8 Ga marine sediments from the Bashkir Meganticlinorium (BMA), Southern Urals, Russia.

45   Our Fe speciation data reveal a water column dominated by ferruginous conditions, no

46   evidence for euxinia, and oxygenated waters confined to only the shallowest, near-coastal

47   settings. Trace metal data support these findings, with Mo and U enrichment factors in anoxic

48   sediments implying the operation of a particulate Fe (oxyhydr)oxide shuttle under ferruginous

49   conditions as the main mechanism for generating moderate authigenic Mo enrichments.

50   Sulfur isotope systematics imply that predominantly low dissolved sulfate concentrations

51   prevailed throughout the deposition of the BMA succession, which, in combination with a low

52   organic carbon loading, promoted the development of ferruginous, rather than euxinic, water

53   column conditions. The restriction of oxic conditions to the shallowest, near-coastal

54   depositional settings within the Bashkir basin contrasts to other redox studies from this period.

55   Such discrepancies highlight major uncertainty in our understanding of the temporal and

56   spatial evolution of water column redox chemistry across the Mesoproterozoic Era, and signify

57　the need for further detailed work to constrain the chemical evolution of the oceans during

58　this crucial time period.

59

1. Introduction

61　　The mid-Proterozoic (~1.8–1.0 Ga) is generally considered an interval of relative

62　environmental and biological stasis. However this assertion may, at least in part, be a

63　consequence of a temporally and spatially limited geochemical record across this vast

64　expanse of time. Canfield (1998) initiated a renewed interest in the evolution of mid-

65　Proterozoic ocean chemistry by proposing that the disappearance of iron formations at ~1.85

66　Ga was due to the development of widespread sulfidic (euxinic) oceanic conditions, rather

67　than the previously envisaged oxygenation of the deep ocean (e.g., Cloud, 1972; Holland

68　1984). The increased potential for euxinia is linked to the first appreciable rise of atmospheric

69　oxygen during the so-called Great Oxidation Event (GOE) at ~2.43–2.06 Ga (Holland, 2002;

70　Luo et al., 2016; Gumsley et al., 2017), fuelled by the enhanced oxidative weathering of

71　terrestrial sulfide-bearing minerals increasing the flux of sulfate to the marine realm. Further

72　investigations have revealed the limited spatial extent of euxinia, indicating that such

73　conditions were confined to productive continental margins and some intracratonic seas

74　(Shen et al., 2002; Shen et al., 2003; Poulton et al., 2004; Gilleaudeau and Kah, 2013; Beghin

75　et al., 2017; Scott et al., 2008). Deeper waters, however, likely remained ferruginous (Poulton

76　et al., 2010; Poulton and Canfield, 2011; Planavsky et al., 2011; Reinhard et al., 2013;

77　Guilbaud et al., 2015; Cox et al., 2016) or possibly suboxic in some regions of the deep ocean

78　(Slack et al., 2007; Slack and Cannon, 2009; Planavsky et al., 2018).

79　　Several recent studies of geographically distinct sedimentary basins have, however,

80　suggested that deeper waters may have been episodically oxic during the mid-Proterozoic

81　(Sperling et al., 2014; Yang et al., 2017; Zhang et al., 2016). Specifically, Sperling et al. (2014)

82　argued for oxic basinal waters based on geochemical data from the ~1.4 Ga Arlan Member

83　of the Kaltasy Formation (Volga-Ural region, Russia); while Zhang et al. (2016) suggested

84　that the ~1.4 Ga Xiamaling Formation (North China Craton) records oxic waters beneath an

85　'oxygen minimum zone' impinging on the shelf. Furthermore, Yang et al. (2017) proposed that

86　less than 25% of the ocean floor was anoxic at ~1.4 Ga based on U isotope data. These

87　observations contrast with detailed studies of other mid-Proterozoic settings (Gilleaudeau and

88   Kah, 2015; Poulton et al., 2004, 2010, Shen et al., 2002, 2003) and, if correct, imply significant
89   spatial and/or temporal heterogeneity in the redox structure of mid-Proterozoic oceans.

90   While there is significant debate over the temporal and spatial evolution of redox conditions
91   in deeper ocean waters, the shallow marine environment is generally considered to have
92   remained oxic since the GOE (Poulton and Canfield, 2011; Li et al., 2015; Cox et al., 2016;
93   Kipp et al., 2017, 2018). Nevertheless, even the extent of shallow water oxygenation in the
94   mid-Proterozoic is rather poorly constrained. For example, the carbon isotope composition of
95   organic matter isolated from ~1.65–1.3 Ga sedimentary rocks from the North China Craton
96   have been interpreted to indirectly reflect a very shallow chemocline (Luo et al., 2014), while
97   rare-earth element (REE) data from the same succession imply very low shallow water O_2
98   concentrations (≤ 0.2 µM; Tang et al., 2016). These observations may be consistent with the
99   suggestion of very low atmospheric oxygen concentrations through the mid-Proterozoic
100   (Planavsky et al., 2014). Conversely, constraints on atmospheric oxygen across this time
101   period vary widely, with recent suggestions of 0.1 to 10% PAL (present atmospheric levels;
102   (Planavsky et al., 2014; Cole et al., 2016; Zhang et al., 2016; Daines et al., 2017; Crockford
103   et al., 2018). In addition, while it is tacitly assumed that atmospheric oxygen concentrations
104   remained relatively constant through the mid-Proterozoic (Canfield, 2005; Lyons et al., 2014;
105   Planavsky et al., 2014), significant fluctuations in atmospheric oxygen remain a distinct
106   possibility (Diamond et al., 2018; Gilleaudeau et al., 2016; Mukherjee and Large, 2016; Yang
107   et al., 2017; Zhang et al., 2016). Given the close link between atmospheric oxygenation and
108   ocean redox conditions, such fluctuations would naturally be expected to drive significant
109   temporal and, potentially, spatial variability in the ocean's redox structure. Indeed, in a
110   detailed study of the ~1.57 Ga Gaoyuzhuang Formation, North China Craton, Zhang et al.
111   (2018) found evidence for a significant oxygenation event that led to the progressive
112   deepening of the oxycline.

113   Given these contrasting views, potentially promoted by a sparse geochemical record, there
114   is clearly a need for further redox appraisals to place unequivocal constraints on the evolution
115   of mid-Proterozoic ocean redox conditions. To address this knowledge gap, we applied a
116   multi-proxy geochemical approach (Fe-S-C systematics and elemental abundances) to
117   reconstruct the prevailing water column redox conditions during the deposition of marine
118   sediments from the ~1.6−0.8 Ga Bashkir Meganticlinorium, Southern Urals. The succession
119   comprises sediments deposited in very shallow (near-coastal) settings through to deeper

120   marine environments, permitting a thorough depth-dependant evaluation of the prevailing
121   redox conditions during this poorly understood interval of Earth's history.

122

123   **2. Geological setting**

124   2.1. Regional geology

125   The Bashkir Meganticlinorium (BMA) comprises a Mesoproterozoic–Neoproterozoic
126   sedimentary and volcano-sedimentary succession. Unconformably overlying the Archean to
127   Paleoproterozoic Taratash Complex, it consists of a series of tectonically stacked
128   allochtonous sheets, thrusted to the west during the Late Palaeozoic Uralian orogeny
129   (Puchkov, 1997; Kuznetsov et al., 2017; Maslov et al., 1997). The BMA is located on the
130   eastern margin of Baltica (Fig. 1), a Precambrian craton assembled in the middle to late
131   Paleoproterozoic from the collision of three continental blocks: Fennoscandia, Sarmatia, and
132   Volga-Uralia (Glasmacher et al., 2004; Lubnina et al., 2016). Though this region has endured
133   several major orogenic events, the strata of the BMA's western limb only experienced deep
134   burial diagenesis (Glasmacher et al., 2004), and were exclusively sampled in this study. The
135   eastern limb was subjected to eclogite-grade metamorphism and is separated from the rest
136   of the BMA by the N-S trending Zuratkul Fault, a major metamorphic and structural boundary
137   between the two limbs (Glasmacher et al., 2001; Giese et al., 1999). This complicated
138   deformational history has further hindered estimates of the units' thicknesses, causing large
139   ranges in the minimum and maximum thickness of each formation as shown in Fig. 2.

140   The BMA consists of four first-order, unconformity-bounded sequences (Shatsky, 1945;
141   Shatsky, 1960). The lower three sequences, each starting with mafic volcanic rocks and
142   conglomerates, fine upwards into shales and carbonates. Together these sequences define
143   the stratotype section of the Riphean, a major Precambrian unit in the Russian stratigraphic
144   nomenclature, lasting from 1750 to 640 Ma (Semikhatov et al., 2015). The 12–15 km thick
145   Riphean deposits of the BMA were deposited along the long-lived, passive continental margin
146   of the Baltica craton since at least ~1380 Ma (Maslov, 2004; Romanyuk et al., 2013; Puchkov
147   et al., 2013). Furthermore, even older, Lower Riphean carbonates of the Satka and Bakal
148   formations have Sr isotope values consistent with a hydrographic connection to the open-
149   ocean (Kuznetsov et al., 2003; Kuznetsov et al., 2008; Semikhatov et al., 2009). Deposition
150   in an open marine setting is supported by a combination of sedimentological and geochemical
151   observations, including: 1) the presence of glauconite in the Middle and Upper Riphean

152 sequences (Keller and Chumakov, 1983); 2) facies changes and mineralogical maturity
153 indicate deepening to the east towards the margin of Baltica; 3) paleocurrent directions
154 denote a westerly source (Akimova, 1967); 4) the large thickness (km-scale) of carbonates
155 and mature composition of sandstones; and 5) Sr isotope values consistent with an open-
156 ocean seawater signal (Semikhatov et al., 2009). By contrast, the ~1.4 Ga Arlan Member of
157 the Kaltasy Formation studied by Sperling et al. (2014) was deposited in the western part of
158 the Kama-Belsk aulacogen of the Volga-Ural region, more than 150 miles to the NW of
159 Baltica's margin, along which the BMA is located. Hence the Kama-Belsk aulacogen of the
160 Volga-Ural region was probably more isolated from the open ocean than the BMA.

161   The Riphean of the BMA is divided into three first-order, unconformity-bound sequences:
162 the Burzyan Group of the Lower Riphean (1.75−1.35 Ga), the Yurmatau Group of the Middle
163 Riphean (1.3−1.0 Ga), and the Karatau Group of the Upper Riphean (1.0–0.65 Ga; Maslov et
164 al., 1997). The stratigraphy of the Bashkir basin and the stratigraphic position of the sampled
165 intervals are shown in Fig. 2. Deposition of the Burzyan and Yurmatau groups started with
166 short periods of rifting, followed by the development of a broader sag basin in which
167 subsidence continued over prolonged periods (Maslov, 2004). A large, shallow marine basin
168 later developed during deposition of the Karatau Group, extending from the Southern to
169 Middle Urals (Maslov et al., 2010). Basal unconformities separate the groups, with coarse
170 siliciclastics marking the base, and marine carbonates occurring at the top of the groups. This
171 upward-deepening cyclicity is a key feature of the Riphean depositional history. The Lower
172 Riphean represents a deepening unit, from fluvial or near-shore conditions to below storm
173 wave base, whereas the Middle and Upper Riphean preserve a more muted deepening,
174 remaining above storm wave base (Maslov, 2004; Kuznetsov et al., 2017). For simplicity,
175 settings above storm wave base will be referred to as shallow marine, and those below the
176 storm wave base as deeper marine. The two main depositional environments present in all
177 three groups of the BMA can be grouped into inner (littoral and sublittoral) and outer (shallow
178 marine) shelf. Evidence for inner shelf deposits includes their predominantly red colour and
179 sedimentary structures such as desiccation cracks, small-scale cross-bedding, and
180 wave/current ripple marks (Maslov et al., 1997). Outer shelf shallow marine sediments show
181 no evidence for subaerial exposure, and contain horizontal, small-scale cross- and planar
182 bedding (Maslov et al., 1997), signifying palaeo-water depths of less than 120 m
183 (Immenhauser, 2009). There is no evidence for turbidite deposition in the BMA succession
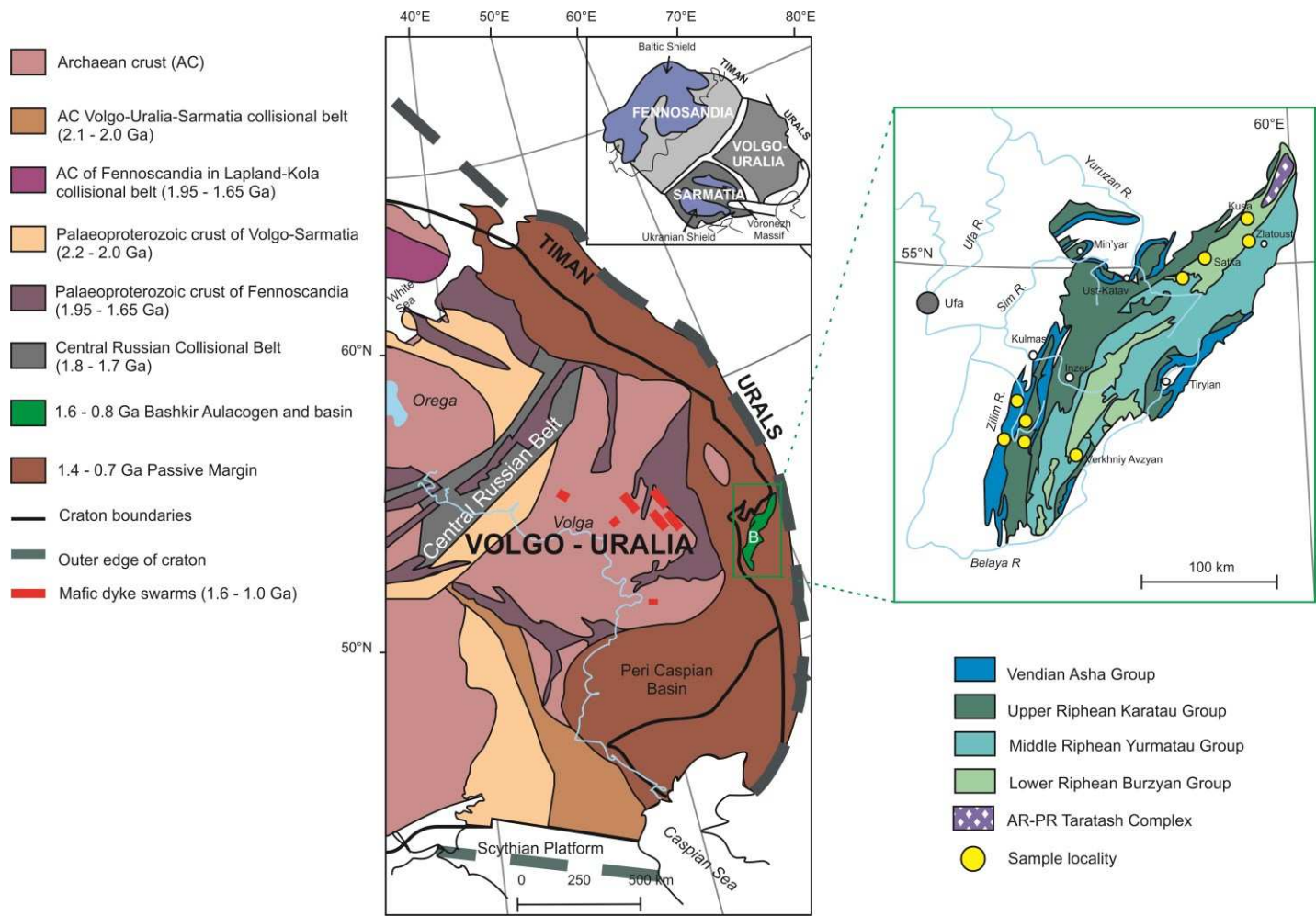184 (Maslov et al., 1997).

Fig. 1. Geological map of the Southern Urals highlighting the position of the Bashkir Meganticlinorium (B), adapted from Puchkov et al. (2013). The inset illustrates the regional geology of the eastern margin of Baltica where the Ural Mountains developed. The geological map of the BMA is adapted from Kuznetsov et al. (2017). Sampling localities are highlighted by yellow circles.

2.2. The Burzyan Group

The Lower Riphean (1.75−1.35 Ga) in the BMA comprises three formations: the Ai, Satka, and Bakal formations (Fig. 2). The lower member of the Ai Formation (not sampled in this study), is a terrestrial deposit of breccias, conglomerates, and sandstones with locally overlying trachybasalts, subalkaline basalts, and tuffs of the Navysh Complex (Krasnobaev et al., 2013; Gorozhanin et al., 2014). This terrestrial-alluvial environment transitioned into a moderately deep marine basin in the upper member, marked by a thick deposit of black shales (Maslov, 2004) that were targeted for the present study. Trachybasalts in the basal part of the Ai Formation (Navysh Complex) gave a U-Pb age of 1752 ± 11 Ma (Krasnobaev et al., 2013). Considering that this alkaline, mafic magmatism occurred shortly after the amphibolite facies metamorphism and granitization of the underlying Archean basement (Krasnobaev et al., 2013), this age constraint might reflect orogen collapse, extension, and development of the successor basin. The overlying Satka Formation consists of five subformations: the Lower and Upper Kusa, Polovinka, and Lower and Upper Satka (Semikhatov et al., 2009). The formation consists predominantly of dolostone, with subordinate interbedded shales and fine-grained siltstones (all sampled for the present study), highlighting the changing depositional conditions. The shales and fine-grained siltstones were deposited below fair weather and storm wave base, with subsequent carbonate deposition occurring between storm wave base and fair weather wave base (Maslov, 2004; Kuznetsov et al., 2008). Conformably overlying the Satka Formation is the Bakal Formation, a shallow marine deposit comprising black shales (targeted for this study), siltstones, and fine-grained sandstones with minor amounts of limestone and dolostone (Maslov et al., 1997, 2012). The formation is subdivided into the Lower Bakal Subformation, an accumulation of grey-black shales deposited in a stagnant, shallow marine basin (Maslov, 2004), and the Upper Bakal Subformation, a carbonate sequence containing a diverse stromatolite assemblage (Semikhatov et al., 2009). A diabase dyke cutting the Bakal Formation yielded a U-Pb baddeleyite age of 1385 ± 1.4 Ma (Ernst et al., 2000), and nepheline syenites of the Berdyaush Massif that intrudes the underlying Satka Formation produced an ID-TIMS U-Pb age of 1368.4 ± 6.2 Ma (Ronkin et al., 2007).

Thickness m	Age			Gr.	Fm.		
100-1000	Neoprot.	Upper Riphean		Karatau	Inz		E 844 ± 24 Ma
250-400					Katav		
900-3050					Zilmerdak		]260 m
1600-2300	Mesoproterozoic	Middle Riphean		Yurmatau	Avzy		]490 m
750-1500					ZK		D 1330 ± 20 Ma
500-700					Zi		
1600-3000					Mashak		]405 m
							C 1386 ± 3 Ma
1500-1650		Lower Riphean		Burzyan	Bakal		]360 m
2500-3500					Satka		B 1550 ± 30 Ma]600 m
1700-2500					Ai		A 1752 ± 11 Ma

Legend:
- Conglomerate
- Sandstone
- Siltstone/Shale
- Limestone
- Dolostone
- Volcanics
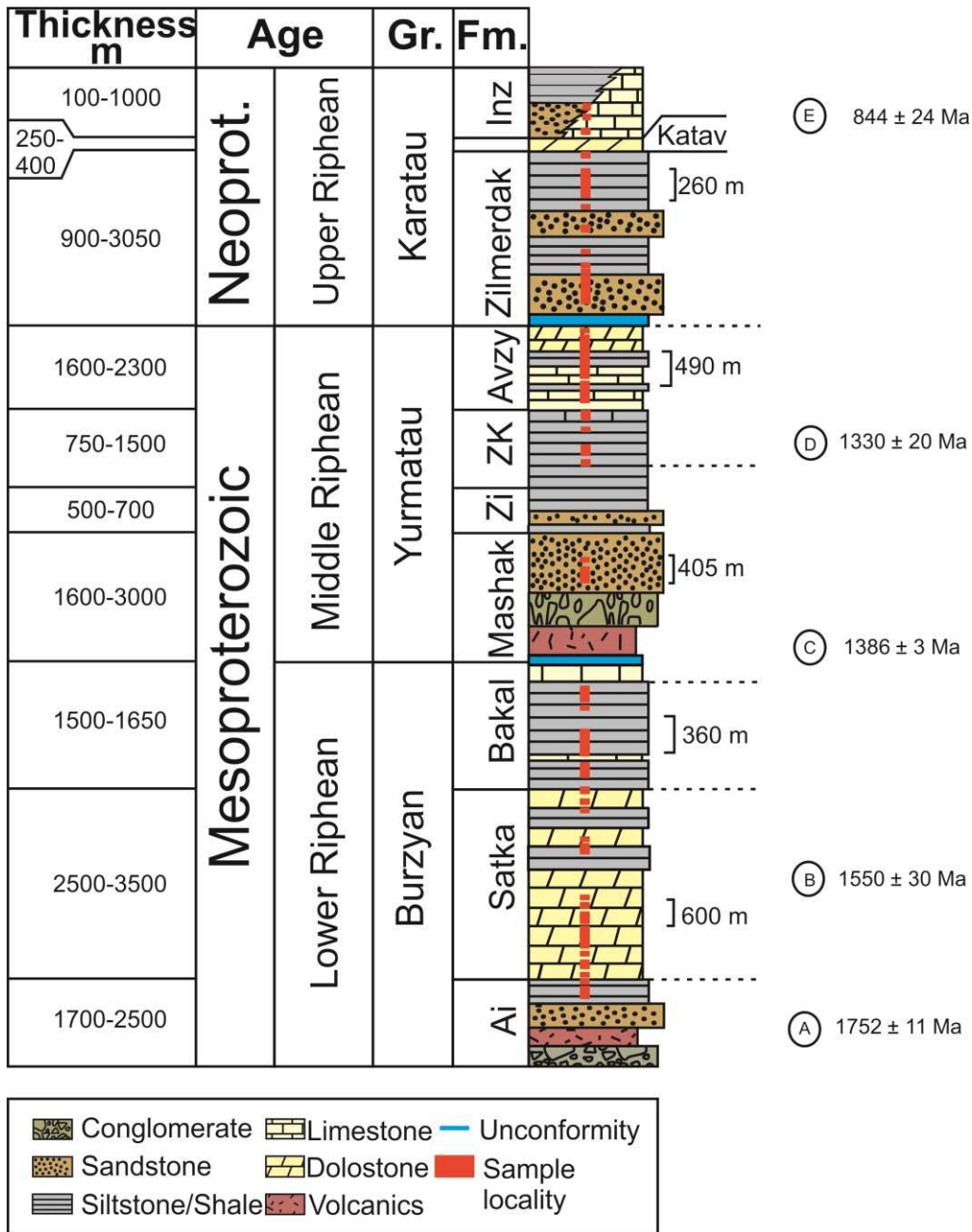- Unconformity
- Sample locality

Fig. 2. Stratigraphic column of the BMA sedimentary succession, adapted from Bartley et al. (2007). Thicknesses taken from Maslov et al. (1997). Scale bars denote thickness used for corresponding samples. Sample positions are shown in red. Gr – Group; Fm – Formation; Zi – Zigalga formation; ZK – Zigazino-Komarovo formation; Avzy – Avzyan formation; Inz – Inzer formation. Between the Zilmerdak and Inzer formations is the Katav Formation. Dating: A – U-Pb zircon age (Krasnobaev et al., 2013); B – Pb-Pb carbonate age (Kuznetsov et al., 2008); C – U-Pb zircon age (Puchkov et al., 2013); D –Pb-Pb phosphorite age (Ovchinnikova et al., 2013); E – Pb-Pb carbonate age (Kuznetsov et al., 2017).

9

214

2.3. The Yurmatau Group

216   The Middle Riphean Yurmatau Group overlies the Burzyan Group with an angular
217   unconformity at its base. It consists of four formations: the Mashak, Zigalga, Zigazino-
218   Komarovo, and Avzyan formations. Rhyolites and dacites at the base of the Mashak
219   Formation gave a U-Pb zircon SHRIMP age of 1386 ± 3 Ma (Puchkov et al., 2013). The lower
220   and middle parts of the Mashak Formation consist of conglomerates and siliciclastics
221   deposited in a near-shore setting within an intracontinental rift basin (Maslov et al., 1997,
222   2012). The upper part of the Mashak Formation, where samples were collected, also consists
223   of siliciclastics, but was deposited in a shallow marine setting. Similarly, the overlying Zigalga
224   Formation, where two samples were taken, is also from a near-shore and shallow marine
225   setting, comprising fine- and medium-grained quartzitic sandstones and siltstones.
226   Siliciclastic deposition continued in the overlying Zigazino-Komarovo Formation with black
227   shales and siltstones, which were sampled for the present study. The Zigazino-Komarovo
228   Formation contains phosphorite nodules, which yielded a Pb-Pb isochron age of 1330 ± 30
229   Ma (Ovchinnikova et al., 2013). Finally, the overlying Avzyan Formation consists of six
230   members, the Kataskin, Malyi Inzer, Ushakov, Kutkur, Revet, and the locally developed
231   Tyulmen members. Five members were sampled for the present study. The formation
232   contains a spectrum of siliciclastic and carbonate rocks deposited in various settings, from
233   shallow marine to near-shore and lagoonal. Desiccation cracks, intraformational breccia, and
234   conglomerate beds point towards a shallow marine setting for the lower Kataskin Member
235   (Bartley et al., 2007), which contains black shale at the base and micritic limestone in the
236   upper part. Subtidal conditions developed during deposition of the middle Malyi Inzer
237   Member, which is composed of thinly bedded shale, suggesting deposition in a low energy
238   environment.

239

2.4. The Karatau Group

241   The Karatau Group includes five formations: the Zilmerdak, Katav, Inzer, Min'yar, and Uk
242   formations. Only the Zilmerdak and Inzer formations were sampled. The Upper Riphean
243   Karatau Group mainly consists of siliciclastics and carbonates, which are exposed on the
244   western limb of the BMA (Kuznetsov et al., 2006, 2017). An angular unconformity separates
245   the Avzyan Formation from the overlying Zilmerdak Formation, marking the boundary

between the Upper and Middle Riphean. The only age constraints for the Karatau Group are from the youngest U-Pb LA-ICP-MS age of detrital zircons isolated from the Zilmerdak Formation (1817 ± 59 Ma; Romanyuk et al., 2013) and Pb-Pb carbonate isochron ages of 844 ± 24 Ma and 820 ± 77 Ma for the Inzer and Min'yar formations, respectively (Kuznetsov et al., 2017). The Zilmerdak Formation is subdivided into four members (Maslov, 2002). The lowermost unit (not sampled) is the Bir'yan Member, consisting of red and light-coloured conglomerates, arkosic to subarkosic sandstones, and siltstones, deposited in a braided river system (Maslov et al., 1997). The overlying Nugush Member is an inner-shelf deposit of grey to dark-grey siltstones, shales and argillites, where eight samples were taken. The overlying Lemeza Member is a light-coloured sandstone unit with thin siltstone beds (not sampled). The uppermost Bederysh Member of sandstones, siltstones and argillites, from which 21 samples were collected, was deposited in a littoral to sublittoral zone, similar to the Nugush Member (Maslov, 2004). Overlying the Zilmerdak Formation is the Katav Formation (not sampled), a shallow marine deposit of red and pink limestones and marls with carbonate flat-pebble breccias and red argillites at the base (Kuznetsov et al., 2017). The uppermost formation sampled in this study (below the predominantly carbonate Min'yar and Uk formations) is the Inzer Formation. This shallow marine unit is predominantly siliciclastic, with minor carbonate horizons. Glauconite is also found at the boundary with the underlying Katav Formation (Maslov, 2004; Kuznetsov et al., 2006).

3. Materials and methods

3.1 Samples

In total, 193 samples from marine formations of the BMA were collected. Sampling locations are shown in Fig. 1. Of these, 54 samples were carbonates and the remaining samples were shales. Excluding the Bakal Formation, which was sampled from a quarry, the remaining samples originated from fresh river cuttings or roadside outcrops. Care was taken to ensure that the freshest samples were collected, avoiding mineral veins and igneous intrusions that could potentially alter the primary geochemical signal. Any weathered surfaces were first cut from hand samples using a slab saw and subsequently crushed to a fine, homogenous powder (<63 μm) with a disc mill.

3.2. Carbon

11

278   Total organic carbon (TOC) and total carbon (TC) were measured on a LECO C-S
279   analyser. The carbonate fraction was removed prior to TOC analysis via two sequential
280   dissolutions with 20% (vol/vol) HCl for 24 hours. Samples were then washed with Milli-Q water
281   until all the remaining acid had been removed (pH > 4) and subsequently dried at 70°C. Total
282   inorganic carbon (TIC) was calculated as the difference between total carbon (TC) and TOC.
283   Samples with greater than 50% TIC (6 wt% $CaCO_3$) were classified as carbonates. The
284   standard Low C soil (Part number 502-062; certified value 1.99 ± 0.04 wt% C) was used for
285   calibration and as an internal standard inserted after every ten unknowns. Replicate analysis
286   (n = 24) yielded a carbon content of 1.95 ± 0.07 wt%, which is statistically indistinguishable
287   from its certified value.

288

289   *3.3 Iron Speciation*

290   Iron speciation is the primary paleo-redox indicator used in this study. This sequential
291   extraction (Poulton and Canfield, 2005) targets iron phases that are considered highly
292   reactive (Fe_{HR}) in terms of (bio)geochemical cycling in anoxic environments (Raiswell and
293   Canfield, 1998). The pool of Fe_{HR} consists of four iron phases: iron carbonate (Fe_{CARB};
294   including siderite and ankerite), ferric iron (oxyhydr)oxide minerals (Fe_{OX}; including hematite
295   and goethite), magnetite (Fe_{MAG}), and iron sulfide phases (Fe_{PY}; dominantly pyrite). Iron
296   carbonate (Fe_{CARB}) was first extracted using Na-acetate at pH 4.5 and 50°C for 48 hours,
297   followed by Fe_{OX} using Na-dithionite for two hours at room temperature, and finally Fe_{MAG}
298   using ammonium oxalate for six hours. Total iron (Fe_T) was determined on ashed (550°C for
299   8 hours) sample aliquots after a HNO_3-HF-$HClO_4$-H_3BO_3 mixed-acid digestion. Poorly
300   reactive sheet silicate Fe (Fe_{PRS}; Raiswell and Canfield, 1996, 1998) was determined via a 1
301   minute boiling HCl extraction (Fe_{HCl}; Raiswell et al., 1994), and was calculated as Fe_{PRS} =
302   Fe_{HCl} – (Fe_{CARB} + Fe_{OX} + Fe_{MAG}). The remaining unreactive silicate Fe (Fe_U) was calculated
303   as Fe_U = Fe_T – Fe_{HR} – Fe_{PRS}. All dissolved Fe concentrations were determined via atomic
304   adsorption spectrometry. Replicate analyses (*n = 6*) gave a RSD of 1.4% for Fe_{CARB}, 1.7% for
305   Fe_{OX}, 3.3% for Fe_{MAG}, and 4.5% for Fe_{PRS}. For Fe_T, replicate analyses (*n = 6*) gave a RSD of
306   2.4%, with 96% recovery for the international sediment standard PACS-2 (certified value =
307   4.09 wt%).

308   Pyrite iron (Fe_{PY}) was determined stoichiometrically by weight from a Ag_2S precipitate
309   formed after a HCl and chromous chloride distillation (Canfield et al., 1986; Poulton and

310   Canfield, 2005). All samples were tested for the presence of acid volatile sulfide

311   (predominantly FeS) via an initial 6M HCl distillation, but in all cases AVS was below

312   detection.

313   Iron speciation uses the ratio Fe_{HR}/Fe_T to assess the redox state of a water column

314   (Raiswell and Canfield, 1998; Raiswell et al., 2001; Poulton and Canfield, 2011). Oxic

315   conditions may be indicated when Fe_{HR}/Fe_T is less than 0.22, while Fe_{HR}/Fe_T ratios exceeding

316   0.38 arise from the additional water column precipitation of Fe_{HR} minerals under anoxic

317   conditions. Fe_{HR}/Fe_T ratios between 0.22 and 0.38 are considered equivocal (Poulton and

318   Canfield, 2011), and may be the consequence of either rapid background sedimentation

319   under anoxic conditions (e.g., turbidite deposition; Canfield et al., 1996), or via the transfer of

320   non-sulfidized Fe_{HR} minerals to poorly reactive sheet silicates (Fe_{PRS}) during diagenesis and

321   burial metamorphism (Poulton and Raiswell, 2002; Poulton et al., 2010; Cumming et al.,

322   2013). Turbidites are not known in the Riphean of the Urals (Maslov et al., 1997) and the

323   conversion of Fe_{HR} to Fe_{PRS} can be evaluated by considering the Fe_{PRS} content of samples

324   (Cumming et al., 2013; Poulton et al., 2010). For samples deposited from anoxic bottom

325   waters, the ratio Fe_{PY}/Fe_{HR} is used to discriminate between ferruginous ($Fe_{HR}/Fe_T > 0.38$;

326    $Fe_{PY}/Fe_{HR} < 0.7$) and euxinic water column conditions ($Fe_{HR}/Fe_T > 0.38$; $Fe_{PY}/Fe_{HR} > 0.7–0.8$)

327   (Poulton et al., 2004; Poulton and Canfield, 2011).

328   Iron speciation has been extensively calibrated in modern and ancient settings (Raiswell

329   and Canfield, 1998; Raiswell et al., 2001; Poulton and Raiswell, 2002), and has been widely

330   applied to siliciclastic sediments. This technique has also recently been calibrated and applied

331   to carbonates, where the approach is considered robust provided that samples contain

332   greater than 0.5 wt% Fe_T (Clarkson et al., 2014). Thus, only samples with $Fe_T > 0.5$ wt% were

333   analysed for Fe speciation. Furthermore, we stress that our carbonate-derived Fe speciation

334   data are used only in support of the siliciclastic data, with all the carbonate analyses giving

335   Fe speciation results that are consistent with our siliciclastic analyses.

336

337   *3.4 Major (Mn, Al) and trace (Mo, U) metals*

338   Utilizing the same HNO_3-HF-$HClO_4$-H_3BO_3 digests used to determine Fe_T, Mn, and Al

339   concentrations using an ICP-OES (Thermo Fisher iCAP 7400), Mo and U were measured via

340   ICP-MS (Thermo Fisher iCAPQc). For Mn, Mo, and U, our focus was on shale samples in

341   order to identify redox-driven enrichments or depletions relative to the detrital input. Trace

342　metal data from carbonate facies are not considered due to the different mechanisms involved

343　in trace metal sequestration between carbonates and shales (cf. Brumsack, 2006). An internal

344　standard spiked with Y was added to a dilution of each digest to monitor the precision of the

345　Mn and Al measurements via ICP-OES. Replicate analyses gave a RSD of 1.4% for Mn and

346　2.0% for Al, while repeat analyses (n=4) of the international standard PACS-2 gave 96.4%

347　recovery for Mn and 101.9% for Al. For Mo and U, samples were spiked with a Rh internal

348　standard and replicate analyses (n=3) gave RSDs of 7.6% for Mo, and 2.3% for U. The higher

349　RSD for Mo arises from the very low concentration of Mo in the sample chosen for replicate

350　analyses, with deviations in small numbers resulting in larger errors. Thus we also consider

351　the uncertainty of the measurement, which is useful for samples with low concentrations. This

352　is determined from the repeated measurement of an internal standard every 10 samples on

353　the ICP-MS and is used to highlight the variation in results about the mean of the internal

354　standard. Our data gave uncertainty measurements of 0.4% for Mo and 2.3% for U.

355

356　*3.5.　Sulfur isotopes*

357　　　The sulfur isotope composition of pyrite ($\delta^{34}S_{py}$) was determined using the Ag_2S

358　precipitates produced during the Fe_{PY} extraction described above. Isotope analyses were

359　performed in Leeds using a GV Isoprime mass spectrometer coupled to an Elementar

360　Pyrocube. Samples were weighed into tin cups and combusted at 1150°C using pure oxygen

361　(N5.0) injected into a stream of CP grade helium. Excess oxygen was removed by reaction

362　with copper wires held at 850°C and water was removed using Sicapent reagent. Sulfur

363　dioxide (SO_2) was separated from other gases via a temperature controlled adsorption-

364　desorption column.

365　　　The $\delta^{34}S$ of the sample was derived from the integrated mass 64 and 66 signals when

366　compared to an independently introduced pulse of SO_2 reference gas (N3.0). This value was

367　calibrated to the international VCDT scale using the lab standard SWS-3A ($BaSO_4$; assigned

368　$\delta^{34}S$ = +20.3‰) and the inter-lab standard CP-1 (chalcopyrite; assigned $\delta^{34}S$ = -4.56‰). The

369　assigned value for SWS-3A was produced by calibrating it against the following international

370　standards (assigned values vs. VCDT in brackets): NBS-127 (+20.3‰), NBS-123 (+17.01‰),

371　IAEA S-1 (-0.30‰), and IAEA S-3 (-32.06‰). Standards were analysed in triplicate and

372　samples in duplicate. Repeat analysis of the standards (n=150) produced a standard

373　deviation of <0.6‰.

374

3.6.   Assessment of pyrite preservation with optical microscopy and SEM

Thin sections for samples from the Zigazino-Komarovo (*n*=6) and Inzer formations (*n*=5) were examined to evaluate pyrite morphology. Pyrite was specifically targeted for mineral analysis to assess the degree of secondary weathering, as its morphology can be affected by oxidation. If a sufficient degree of oxidation has occurred, an iron oxyhydroxide coating is typically found surrounding the pyrite grains, if not completely replacing the mineral (Williamson and Rimstidt, 1994; Huminicki and Rimstidt, 2009; Gartman and Luther, 2014). Prior to analysis on a Tescan VEGA3 XM scanning electron microscope (SEM), each thin section was carbon-coated to avoid charging the non-conductive rock samples. An energy dispersive x-ray (EDX) analyser was used for elemental identification and compositional information.

386

4. Results

4.1. Evaluating the effect of secondary weathering

Although every effort was made to ensure that only pristine samples were analysed, it is important to evaluate any potential oxidative weathering given that it may alter the geochemical redox data. Fig. 3a shows a representative image of euhedral pyrite in a carbonate sample from the Inzer Formation (14,577 m), which shows no evidence for dissolution features or alteration products. Similar occurrences of euhedral pyrite grains were found in other thin sections, suggesting limited conversion of pyrite to iron oxides. In one instance only, a single band of jarosite was found in a shale from the Zigazino-Komarovo Formation (9,563 m) (Fig. 3b), which may represent a secondary oxidation product of pyrite (cf. Raiswell and Canfield, 2012). Thus, the SEM and EDX spectra indicate that our Fe speciation data have not been significantly compromised by oxidative weathering.
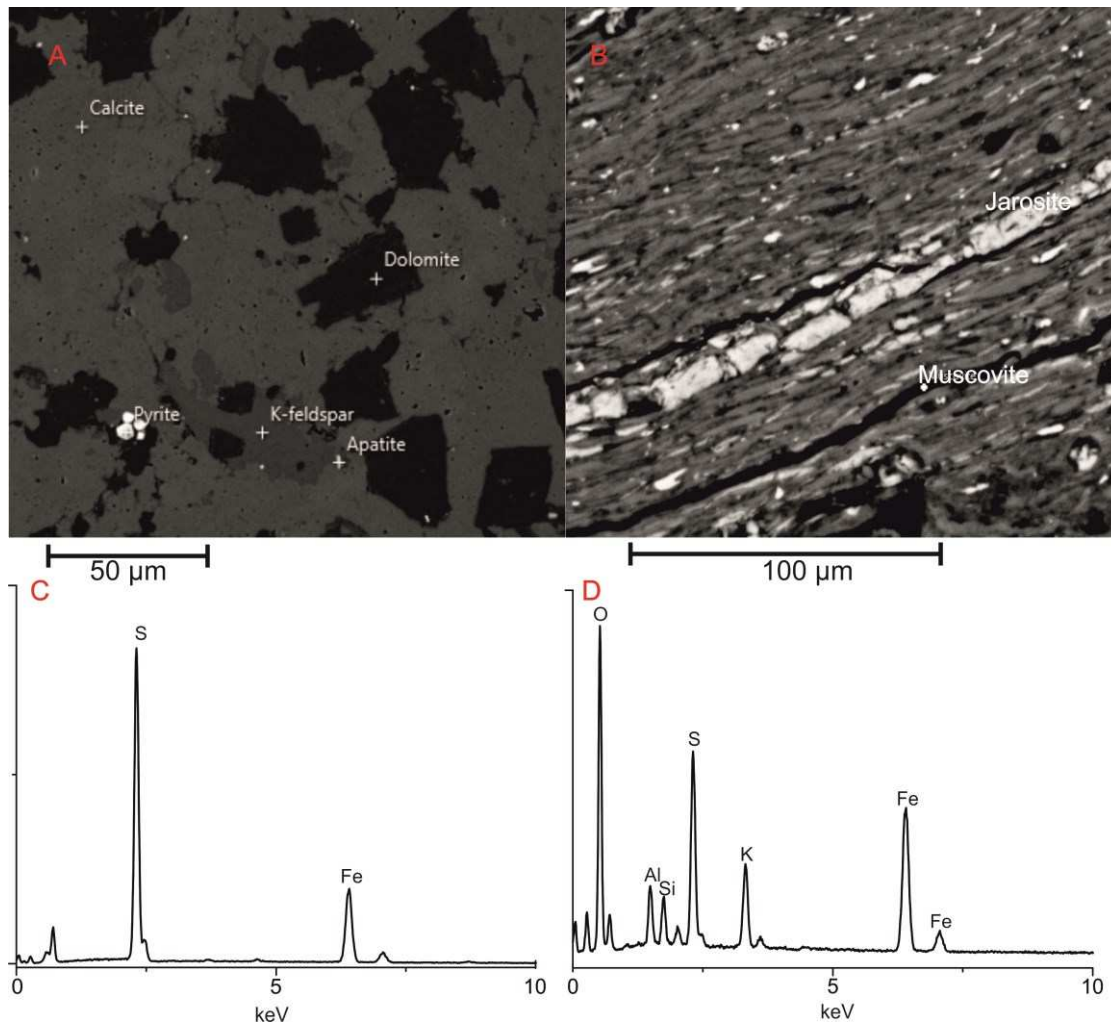
Fig. 3. Representative SEM images. A. Backscatter image of euhedral pyrite in a carbonate sample from the Inzer Formation (14,577 m). B. Backscatter image showing a single occurrence of a jarosite (oxidized pyrite) band of ~10 µm thickness in a shale sample from the Zigazino-Komarovo Formation (9,563 m). C. EDX spectra of euhedral pyrite found in A. D. EDX spectra of jarosite found in B.

399

400   *4.2. Fe-S-C systematics*

401   All geochemical data are reported in Appendix A. Fig. 4 displays the major element and Fe
402   speciation data in a stratigraphic context, alongside a facies-based reconstruction of changes
403   in depositional environment, where shallow water environments are considered to be above
404   storm wave base, and deeper water sedimentation occurred below storm wave base (>120
405   m depth; Maslov et al., 1997; Maslov, 2004, 2002). Carbonate-rich sediments were analysed
406   from four stratigraphic levels in the succession. In each case, interbedded shales were also

16

407   analysed and gave consistent redox results. Organic C is low throughout the succession, with

408   an average of 0.02 ± 0.01 wt% and no systematic variability up-section.

409   Most samples have Fe_T contents greater than 0.5% (Fig. 4) and are thus ideal for Fe

410   speciation. The few samples where Fe_T is below 0.5 wt% were excluded from Fe speciation

411   analysis (Clarkson et al., 2014). A preliminary evaluation of water column redox is given by

412   the Fe_{HR}/Fe_T profile, with the data colour coded to highlight oxic (Fe_{HR}/Fe_T <0.22), equivocal

413   (Fe_{HR}/Fe_T 0.22–0.38), and anoxic (Fe_{HR}/Fe_T >0.38) samples. The sediments of the Lower

414   Riphean show little evidence for oxic depositional conditions, and instead the majority of shale

415   and carbonate samples show persistent evidence for anoxia, with some samples falling in the

416   equivocal zone. In all cases, Fe_{PY}/Fe_{HR} ratios are very low, suggesting ferruginous

417   depositional conditions. Evidence for anoxia persists from the deeper upper member of the

418   ~1.75 Ga Ai Formation, throughout the shallow marine Satka and Bakal formations. For the

419   unconformably overlying Middle Riphean Yurmatau Group, Fe_{HR}/Fe_T ratios suggest oxic

420   water column conditions in the near-coastal Mashak Formation at ~1.38 Ga. These very

421   shallow water sediments feature some of the highest Fe_T values in the succession, up to 11

422   wt% with an average of 6.9 ± 1.9 wt%. Samples with such high Fe_T contain relatively low Fe_{HR}

423   content, thus demonstrating that their iron content predominantly consists of Fe_U or Fe_{PRS}

424   phases. Variable redox conditions developed during deposition of the Zigalga, Zigazino-

425   Komarovo, and Avzyan formations, in concert with fluctuations in water depth. Where anoxic

426   depositional conditions are indicated, almost all samples have Fe_{PY}/Fe_{HR} ratios consistent

427   with ferruginous depositional conditions, although a few samples have higher Fe_{PY}/Fe_{HR} ratios

428   which may reflect either intermittent euxinia or extensive pyritization of the Fe_{HR} pool during

429   early diagenesis (Poulton and Canfield, 2011). Sediments from the shallow marine, upper

430   Zilmerdak Formation show abundant evidence for anoxic, ferruginous depositional conditions.

431   However, some samples from this formation, and most of the samples from the upper part of

432   the Karatau Group, plot in the equivocal range.

433   To evaluate the potential for transfer of unsulfidized Fe_{HR} to Fe_{PRS} in these low-sulfide

434   sediments, ($Fe_{HR}+Fe_{PRS})/Fe_T$ ratios are plotted stratigraphically in Fig. 4. This identifies

435   samples that plot above the average Palaeozoic shale value (0.39 ± 0.11 wt%; Raiswell et

436   al., 2008). In the Lower Riphean, the majority of samples with equivocal Fe_{HR}/Fe_T ratios (0.22–

437   0.38) plot above the upper limit of the Palaeozoic average, indicating that they have

438   significantly elevated Fe_{PRS} contents relative to average Palaeozoic shale. In the Lower Satka

439   Formation, oxic and Fe_{HR}/Fe_T-equivocal samples have ($Fe_{HR}+Fe_{PRS})/Fe_T$ ratios within the

440   limits of average Palaeozoic shale. In the Middle Riphean succession, the near-coastal

441   Mashak Formation contains several samples originally classified as oxic. Half of these

442   samples possess $(Fe_{HR}+Fe_{PRS})/Fe_T$ ratios analogous to average Palaeozoic shale, while the

443   remainder have elevated $(Fe_{HR}+Fe_{PRS})/Fe_T$ ratios. The majority of the remaining oxic samples

444   in this group plot below the lower limit for average Palaeozoic shale. One anoxic and several

445   equivocal Middle Riphean samples are also below this limit. Equivocal shallow water samples

446   from the Upper Riphean also contain relatively high concentrations of Fe_{PRS}.

447   In general, $\delta^{34}S_{py}$ values are enriched in ^{34}S throughout much of the succession, with

448   limited variability and no clear trend in relation to depositional setting (Fig. 4). In the Lower

449   Riphean, $\delta^{34}S_{py}$ values average (n=16) 12 ± 8‰, which is similar to the average and the range

450   of values observed in the Middle Riphean (n=28; 15 ± 8‰). Although there is limited data for

451   the Upper Riphean, these data show more variability, with values as low as -31.8‰ and an
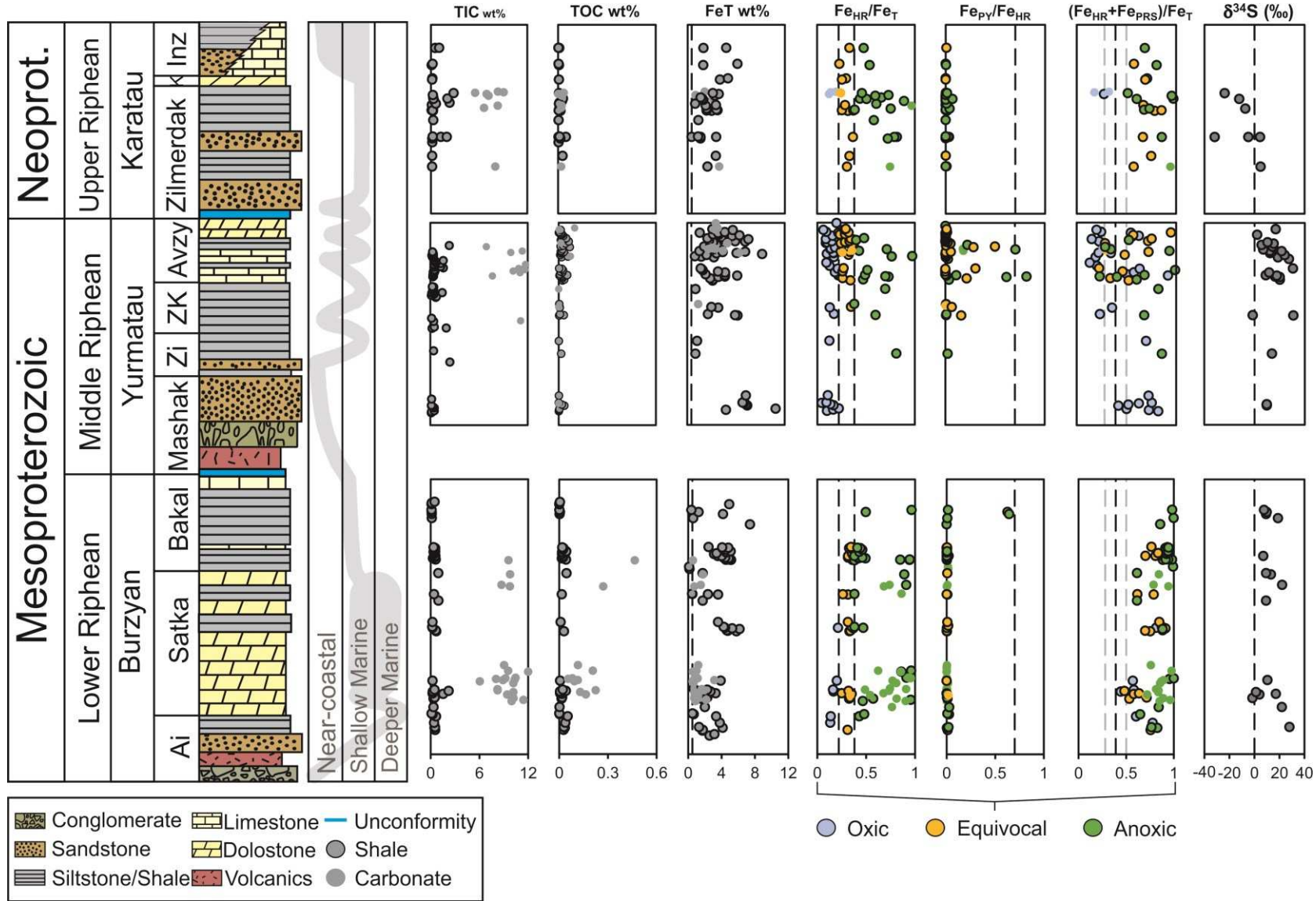
452   average (n=7) of -9 ± 14‰.

18

Fig. 4. Litho- and chemostratigraphic section showing TIC, TOC, Fe_T, Fe_{HR}/Fe_T, Fe_{PY}/Fe_{HR}, $(Fe_{HR}+ Fe_{PRS})/Fe_T$, and $\delta^{34}S_{py}$ data. Iron speciation data are colour-coded based on their inferred redox state. Fe_{PY}/Fe_{HR} ratios are only shown for anoxic and equivocal samples as this ratio does not provide information on water column chemistry to infer oxic water column conditions. The dashed line on the Fe_T plot is at 0.5 wt%, below which samples were not analysed for Fe speciation. Dashed lines on the Fe_{HR}/Fe_T plot distinguish oxic ($Fe_{HR}/Fe_T < 0.22$) from anoxic ($Fe_{HR}/Fe_T > 0.38$) depositional conditions. Dashed line on the Fe_{PY}/Fe_{HR} plot distinguishes ferruginous ($Fe_{PY}/Fe_{HR} < 0.7$) from euxinic ($Fe_{PY}/Fe_{HR} > 0.7$) water column conditions. Dashed lines on the $(Fe_{HR}+ Fe_{PRS})/Fe_T$ plot show the Palaeozoic range (average $\pm$ 1 σ) from Raiswell et al. (2008). The range of inferred depositional environments for each formation is based on facies analysis and adapted from Bartley et al. (2007), Maslov et al. (1997), and Maslov (2002, 2004).

453

4.3. Trace metals

455   Sedimentary Mo, U, and Mn concentrations are shown in Fig. 5, where the dashed lines
456   represent the Average Shale (AS) values from Turekian and Wedepohl (1961). Moderate
457   enrichments are evident for Mo, with the majority of shales from shallow and deep marine
458   settings plotting above the 2.6 ppm average. However, a significant proportion of samples
459   also plot below this average. The plot of U depicts no overall enrichment, with only four
460   samples plotting slightly above AS value. The plot of Mn concentrations illustrates that the
461   majority of the samples are depleted in Mn relative to AS (850 ppm), with a few samples
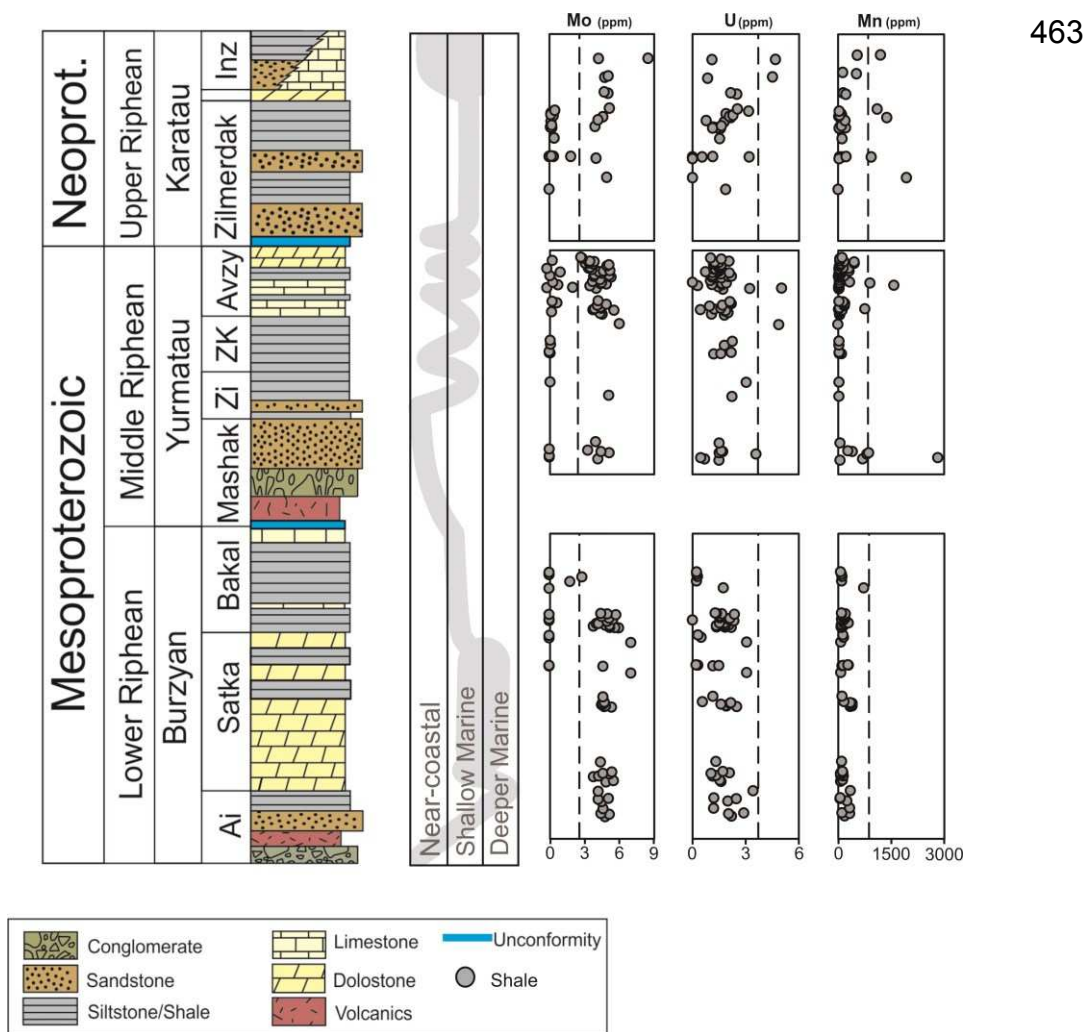462   sporadically plotting above this value.

463

Fig. 5. Litho- and chemostratigraphic variations in concentrations of Mo, U, and Mn (in ppm). Dashed lines represent Average Shale (AS) values from Turekian and Wedepohl (1961). Sources for the stratigraphic column, sea-level variations, and abbreviations are in Fig 2.

5. Discussion

5.1. Ocean redox reconstruction from Fe speciation

To fully evaluate the dominant redox state of the water column throughout the extended period of time recorded by the BMA sediments, we first consider the potential conversion of unsulfidized Fe_{HR} to Fe_{PRS}. Where sulfide production was limited, either because of low sulfate concentrations or low organic matter availability (as is clearly the case for the BMA; Fig. 4), there remains the possibility that dissolved Fe^{2+} sourced from Fe_{HR} during early diagenesis may have been incorporated into clay minerals instead of precipitating as pyrite (Poulton et al., 2010; Cumming et al., 2013; Tosca et al., 2016). Fig. 4 demonstrates that a significant number of Fe_{HR}/Fe_T-equivocal samples and some 'oxic' samples (based on a strict interpretation of Fe_{HR}/Fe_T ratios alone), have $(Fe_{HR}+Fe_{PRS})/Fe_T$ ratios that are well above the upper limit for the Palaeozoic average shale, suggesting a likely transformation of Fe_{HR} to Fe_{PRS}. We evaluate this quantitatively by defining a conservative Fe_{HR}/Fe_T* ratio that incorporates the potential transfer of Fe_{HR} to Fe_{PRS}:

$$\frac{Fe_{HR}}{Fe_T}* = \frac{Fe_{HR}}{Fe_T}meas + (\frac{Fe_{PRS}}{Fe_T}meas - \frac{Fe_{PRS}}{Fe_T}PAS) \qquad (1)$$

where $(Fe_{HR}/Fe_T)_{meas}$ is the measured Fe_{HR}/Fe_T ratio, Fe_{PRS}/Fe_{Tmeas} is the measured Fe_{PRS}/Fe_T ratio, and $(Fe_{PRS}/Fe_T)_{PAS}$ is the upper limit for the Palaeozoic average shale (0.5 wt%) as quantified by Raiswell et al. (2008). Equation 1 was applied to all oxic and equivocal samples from the BMA to evaluate whether any significant loss of Fe_{HR} to Fe_{PRS} may have altered the primary depositional redox signal. This approach has an underlying assumption that the fine-grained sediments are not dominated by juvenile, unweathered materials. We stress here, however, that while this refines our redox interpretations and makes our observations more consistent throughout the succession, it does not lead to any significant change in our overall conclusions. Shown in Fig. 6 are the consequential differences between the original Fe_{HR}/Fe_T values (Fig. 6A) and the incorporation of the new Fe_{HR}/Fe_T* ratio into these results for the appropriate samples (Fig. 6B). There is little change in the percentage of samples with an oxic signal across all depositional environments between these two graphs. The most significant difference is observed in the percentage of redox-equivocal and anoxic samples from shallow and deep marine environments. Employing the original Fe_{HR}/Fe_T ratio, 34% of shallow marine and 38% of deep marine samples were identified as Fe_{HR}/Fe_T equivocal (Fig. 6A). Based on the new approach, these values decrease to 27% and 32%, respectively. As a result, the proportion of anoxic samples rises in both depositional

22

environments. Initially, 49% of both shallow and deep marine samples had Fe_{HR}/Fe_T ratios greater than 0.38, but by correcting for the potential loss of Fe_{HR} to Fe_{PRS} with Equation 1, these values increase to 57% for both settings. The inclusion of Fe_{PRS} into our redox interpretation as shown in Fig. 6B further supports our interpretation of how water column redox conditions varied from near-coastal settings, through shallow marine environments (above storm wave base), and into the deeper, basinal (below storm wave base) settings. We find a clear trend whereby near-coastal settings were dominantly oxic, whereas shallow and deeper marine settings were dominantly anoxic, highlighting that oxic conditions were generally restricted to only the shallowest waters.
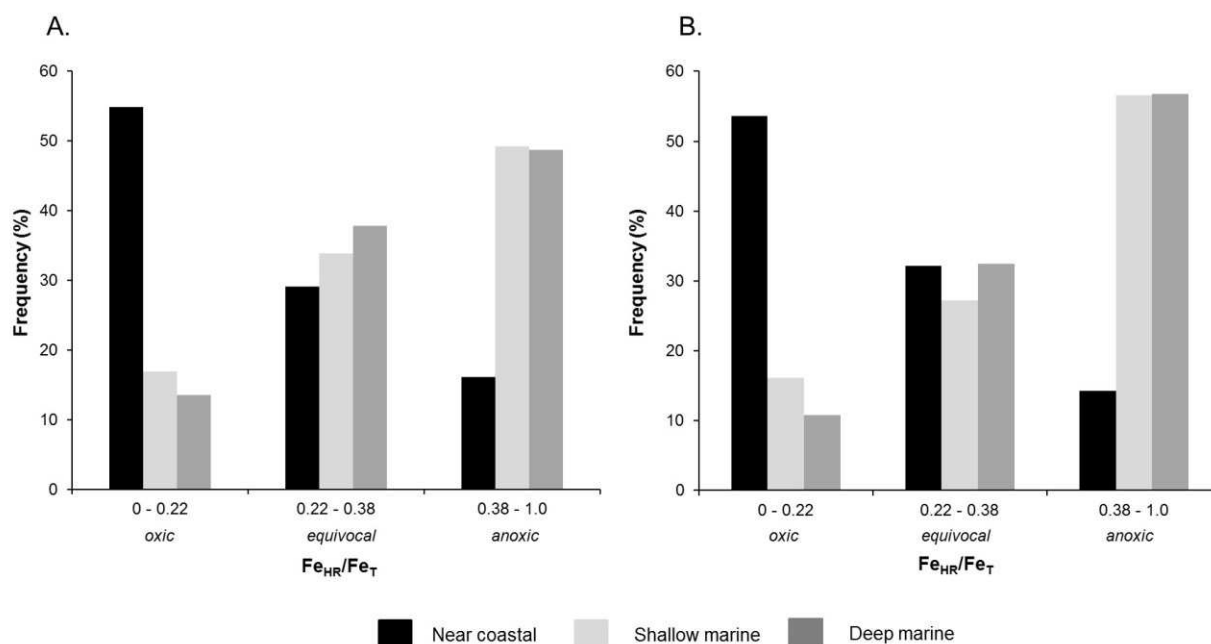
Fig. 6. Frequency plot of Fe_{HR}/Fe_T ratios for near-shore, shallow marine, and deeper marine samples, binned in terms of oxic, equivocal, and anoxic depositional settings. A: Fe_{HR}/Fe_T ratios for each sample B: Fe_{HR}/Fe_T* ratios were used for samples with Fe_{PRS}/Fe_T values above the Palaeozoic average shale (for correction procedure see the main text).

5.2. Redox-sensitive metals

Redox-sensitive metals provide further insight and support for our evaluation of water column redox conditions. To assess the degree of enrichment or depletion relative to average shale we recast the data in Fig. 5 in terms of Enrichment Factors (EF) relative to AS (Algeo

23

510 and Tribovillard, 2009; Brumsack, 2006; Tribovillard et al., 2012), where the EF for a given
511 element (X) is calculated as:

$$X_{EF} = \frac{\frac{X}{Al}sample}{\frac{X}{Al}PAAS} \qquad (2)$$

513   Enrichment factors are plotted stratigraphically in Fig. 7. Here, a value above 1 represents
514 an enrichment and a value less than 1 denotes a depletion, relative to AS. The data show
515 considerable overlap in terms of the oxic, equivocal, and anoxic depositional conditions
516 identified by Fe speciation. However, there are distinct differences between the oxic and
517 anoxic samples, with an average Mo_{EF} for oxic samples of 1.1, whereas anoxic samples have
518 an elevated average Mo_{EF} of 3.3. This difference reflects the contrasting behaviour of Mo
519 under different redox states. Molybdenum initially enters the ocean as the molybdate anion
520 (MoO_4^{2-}) derived from oxidative weathering of continental crust (Bertine and Turekian, 1973).
521 In oxic settings, molybdate is largely unreactive and is removed to the sediments through the
522 slow uptake by Fe-Mn (oxyhydr)oxide minerals (Bertine and Turekian, 1973). Thus, the
523 average Mo_{EF} of 1.1 from our shallow water samples is entirely consistent with dominantly
524 oxic water column conditions in the shallow ocean.

525

526

527

528

529
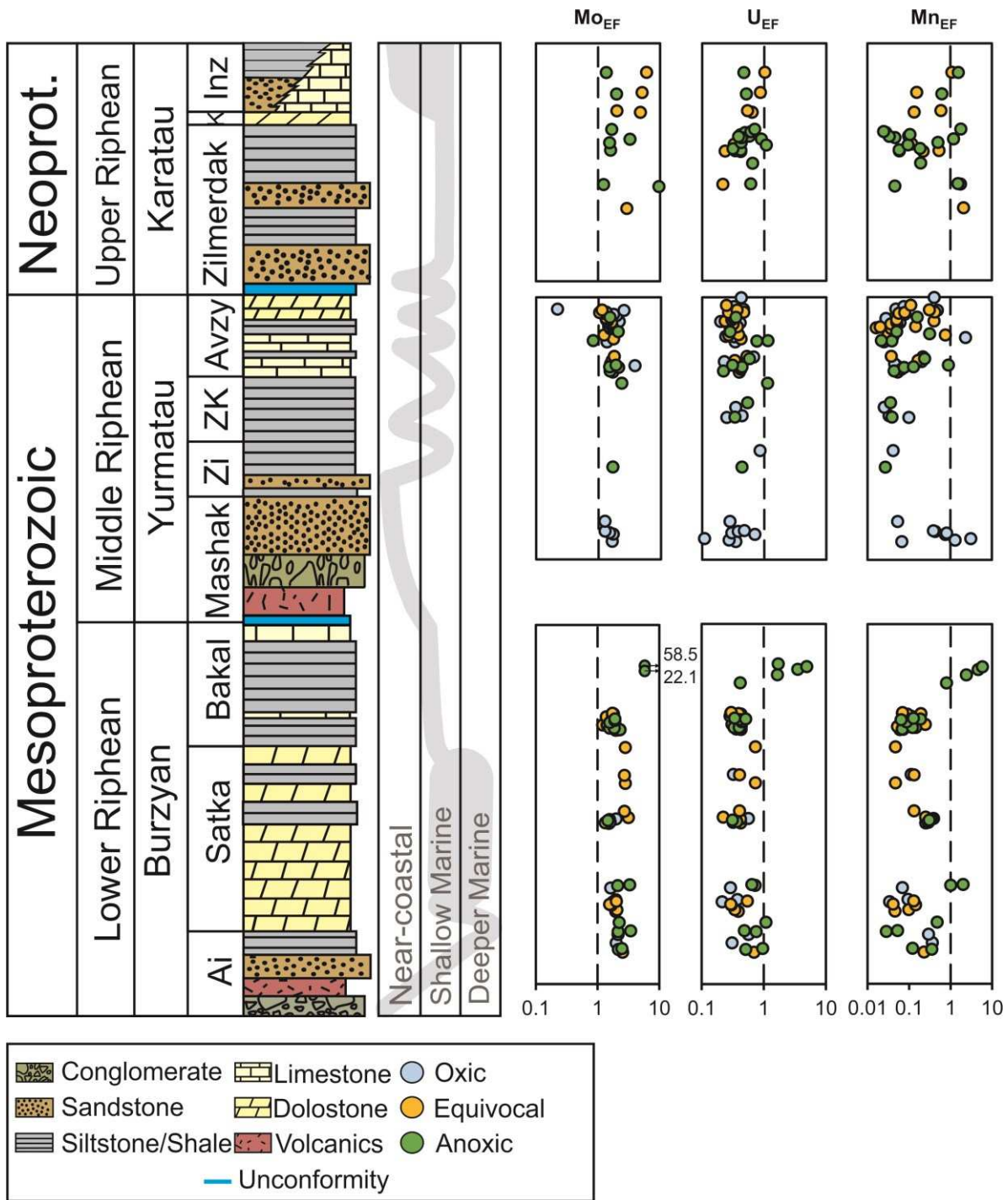
Fig.7. Litho- and chemostratigraphic log of Enrichment Factors for Mo, U, and Mn. Dashed lines at 1 represent the AS reference (Turekian and Wedepohl, 1961). The data points are colour coded according to the prevailing redox conditions inferred from the iron speciation data; blue for oxic, yellow for equivocal, and green for anoxic. Fe_{HR}/Fe_T* ratios were used for the samples with elevated Fe_{PRS}/Fe_T ratios (for correction procedure see the main text).

530

25

By contrast, if a critical threshold of free H_2S is met under anoxic conditions, the molybdate anion is converted to particle-reactive thiomolybdate ($MoO_xS_{4-x}^{2-}$, where x is from 0 to 3; Helz et al., 1996). Under such conditions in modern environments, sedimentary Mo removal is 200 to 5000 times more efficient than under oxic conditions (Scott et al., 2008), leading to significant Mo enrichments (Scholz et al., 2013; Erickson and Helz, 2000; Emerson and Huested, 1991; Helz et al., 1996). Sedimentary Mo enrichments generally scale with sulfide availability. The lower levels of enrichment tend to occur where H_2S is restricted to porewaters, whereas the more extreme enrichments are associated with high levels of water column sulfide (Scott et al., 2008). However, it should also be noted that widespread euxinia can lead to significant depletion of Mo in the global ocean or restricted basin, giving rise to muted sedimentary enrichments even under highly euxinic conditions (Emerson and Huested, 1991; Algeo, 2004; Algeo and Lyons, 2006; Scott et al., 2008; Tribovillard et al., 2012; Goldberg et al., 2016; Thomson et al., 2015). Despite this behaviour, Mo enrichments tend to be orders of magnitude higher in euxinic Mesoproterozoic and Paleoproterozoic settings than the relatively minor enrichments we observe in the anoxic BMA sediments (Scott et al., 2008; Planavsky et al., 2018; Asael et al., 2018). This can therefore rule out widespread euxinia as a cause for Mo enrichments in the results presented here. In addition, Guilbaud et al. (2015) demonstrated a global contraction of euxinic settings in the early Neoproterozoic, coincident with deposition of the Upper Riphean sediments of the BMA. Therefore, the low Mo enrichments observed here are unlikely to have arisen due to the expansion of euxinia elsewhere in the global ocean.

To further evaluate the potential mechanisms involved in Mo drawdown to the sediments under anoxic conditions in the Bashkir basin, we consider the contrasting redox-dependent behaviour of U. A large proportion of the samples are relatively depleted in U (Fig. 7), although as with Mo, there is a clear difference between oxic, shallow water and anoxic, deeper water settings (average oxic U_{EF} = 0.36; average anoxic U_{EF} = 0.73). Unlike Mo, U is preferentially buried in sediments deposited beneath anoxic bottom waters regardless of whether euxinic or ferruginous conditions dominate, as U reduction primarily occurs in the sediments, not in the water column (Anderson et al., 1989; Klinkhammer and Palmer, 1991; Partin et al., 2013). This behaviour is evident as higher enrichments are found in deeper water settings, consistent with anoxic depositional conditions in the basin and, more broadly, low-oxygen conditions in the global ocean.

563   A plot of Mo$_{EF}$ as a function of U$_{EF}$ (Fig. 8) provides information on the mechanisms

564   responsible for sedimentary Mo and U enrichments. Particulate molybdate scavenging in the

565   water column accelerates the accumulation of authigenic Mo relative to other trace metals,

566   such as U, which are not so readily scavenged (Algeo and Tribovillard, 2009).

567   Notwithstanding the possibility that the detrital sediments of the Bashkir basin may have

568   contained relatively low U relative to AS, Fig. 8 clearly demonstrates the preferential

569   enrichment of Mo relative to U. The comparison of sedimentary Mo$_{EF}$:U$_{EF}$ ratios from different

570   contemporaneous redox settings with the modern seawater Mo:U [(Mo:U)$_{SW}$] ratio can help

571   discriminate between different enrichment mechanisms. For example, sediments deposited

572   beneath a suboxic water column in the modern-day tropical East Pacific are enriched in U

573   relative to Mo, and thus feature a low Mo$_{EF}$:U$_{EF}$ (~0.1 to 0.3) relative to (Mo:U)$_{SW}$ (Tribovillard

574   et al., 2012). A progressive shift favouring Mo over U enrichment moves the sedimentary

575   Mo$_{EF}$:U$_{EF}$ ratio toward the seawater ratio, signalling a shift to more intense and stable anoxic

576   water column conditions. Further Mo enrichment, resulting in Mo$_{EF}$:U$_{EF}$ ratios greater than the

577   equivalent seawater ratio, implies the operation of an Fe-Mn (oxyhydr)oxide particulate

578   shuttle for Mo sequestration under anoxic (but not euxinic) water column conditions

579   (Tribovillard et al., 2012). More pronounced Mo enrichment and higher Mo$_{EF}$:U$_{EF}$ ratios are

580   typically the product of euxinic water column conditions, catalysed by the formation of particle-

581   reactive thiomolybdate.

582   As the majority of samples from the BMA plot above the (Mo:U)$_{SW}$ ratio (Fig. 8), and iron

583   speciation data denotes anoxic but not euxinic water column conditions (Figs. 4 and 6), our

584   data favour an Fe-Mn (oxyhydr)oxide particulate shuttle as a Mo enrichment mechanism

585   rather than euxinic sedimentation. In Fig. 8, the green ellipsoid highlights the field of the

586   modern Cariaco basin sediments, where scavenging by Fe-Mn (oxyhydr)oxides promoted the

587   accumulation of Mo in the sediments (Tribovillard et al., 2012). However, the original data for

588   these Cariaco Basin samples do not solely plot in this field, but show a large degree of scatter,

589   with the majority of values greater than the (Mo:U)$_{SW}$ (Algeo and Tribovillard, 2009). Only two

590   samples from the BMA plot in this area, and these are from the Lower Riphean Bakal

591   Formation. These samples have elevated Fe$_{PY}$/Fe$_{HR}$ ratios (Fig. 4), suggesting that increased

592   sulfide availability rather than an intensified Fe-Mn (oxyhydr)oxide shuttle likely stimulated Mo

593   accumulation in these isolated cases. Sulfide availability, however, was generally low

594   throughout deposition of most of the succession, as testified by the low Fe$_{PY}$/Fe$_{HR}$ ratios (Fig.

595   4). Scott et al. (2008) highlighted that Mo concentrations in the mid-Proterozoic ocean were

596 likely significantly lower than at present. Hence, Mo uptake by Fe-Mn (oxyhydr)oxides would

597 be expected to result in lower Mo_{EF}:U_{EF} than in modern anoxic settings, as observed for our

598 samples (Fig. 8). Therefore, Mo drawdown by an Fe-Mn (oxyhydr)oxide shuttle was likely the

599 main mechanism for Mo sequestration beneath the ferruginous water column of the BMA.
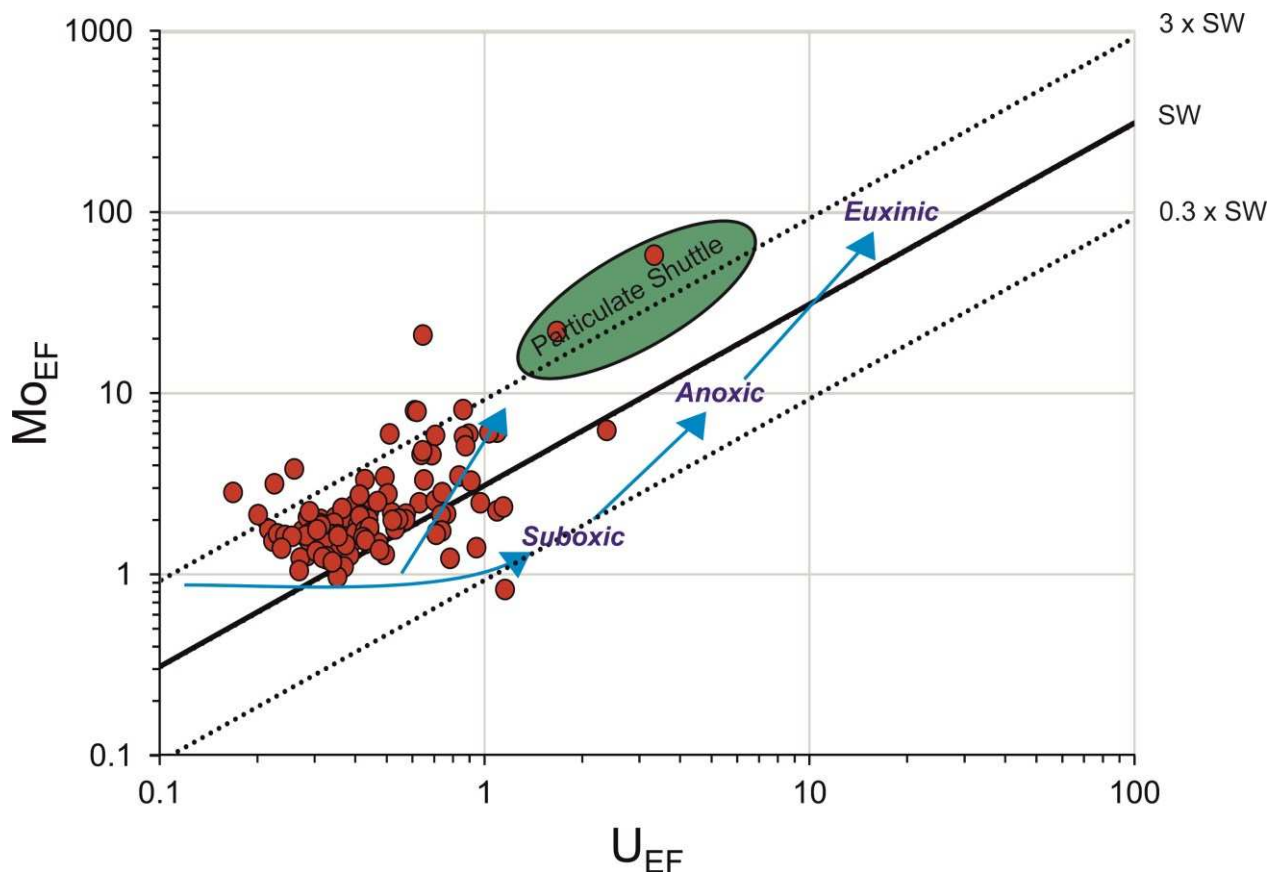
Fig. 8. Plot of Mo_{EF} vs. U_{EF} for shales (red circles) from the BMA. The diagram is modified from Algeo and Tribovillard (2009) and Tribovillard et al. (2012) to accommodate the low levels of U ($U_{EF}<1$). The modern seawater molar Mo/U ratio, $(Mo/U)_{SW}$, of 3.1 (Tribovillard et al., 2012) is represented by the solid black line. The dashed lines correspond to multiples of the $(Mo/U)_{SW}$ ratio. All redox labels were defined for modern environments in open-marine basins by Tribovillard et al. (2012). The arrow pointing to the particulate shuttle highlights how sedimentary Mo_{EF} and U_{EF} would evolve under the operation of an Fe (oxyhydr)oxide particulate shuttle.

600

601 Consistent with a ferruginous water-column in all but the shallowest waters, Mn tends to

602 be depleted throughout much of the succession (Fig. 7), due to the higher redox potential of

603 the Mn(II)/Mn(IV) couple relative to the Fe(II)/Fe(III) couple. This is in stark contrast to the

enrichments commonly evident in unsulfidized Fe$_{HR}$ (Fig. 4), suggesting that Fe (oxyhydr)oxide minerals were the dominant supplier of Mo to the sediment. Thus, the contrasting behaviours of Mo, U, and Mn are entirely consistent with the redox interpretation derived from our Fe speciation data.

5.3. Spatial and temporal variability in mid-Proterozoic ocean redox chemistry

Our Fe-speciation and trace-metal data strongly suggest that below a very shallow chemocline, waters were dominantly anoxic and ferruginous. We further evaluate potential controls on the widespread development of ferruginous, rather than euxinic, water column conditions in the Bashkir basin by considering sulfur isotope systematics. The isotopic composition of seawater sulfate is poorly constrained throughout the Mesoproterozoic and early Neoproterozoic, but low resolution estimates from carbonate-associated sulfate suggest a likely range of ~25–35‰ (Guilbaud et al., 2015; Kah et al., 2004; Turner and Bekker, 2016). Pyrite-derived S isotope values average 11.8 ± 8.0‰ for the Lower Riphean and 15 ± 8‰ for the Middle Riphean (Fig. 4), giving enrichment factors from seawater sulfate of around 15–25‰. Given the low pyrite content of these sediments, this suggests that the extent of S isotope fractionation imparted during bacterial sulfate reduction was subdued due to low seawater sulfate concentrations in this particular basin (Canfield, 2000; Habicht et al., 2002).

Following the GOE, the onset of oxidative continental weathering, and thus an increase in the flux of sulfate to the ocean, is supported by the disappearance of detrital pyrite from sediments (Holland, 2002; Bekker et al., 2004) and a dramatic decrease in δ^{34}S values after the disappearance of Δ^{33}S (Bekker et al., 2004; Luo et al., 2016; 2018). There is currently no direct, uncontested evidence for a further, long-term rise in atmospheric oxygen until the Late Neoproterozoic. Estimates for Mesoproterozoic atmospheric oxygen partial pressure (ρO$_2$) suggest a decline to levels between ~0.01 to 0.1 PAL following the Lomagundi Event, with persistent low values until the Late Neoproterozoic (Daines et al., 2017; Bellefroid et al., 2018; Crockford et al., 2018). Since there was limited, if any, variation in the terrestrial flux of sulfate to the oceans in the aftermath of the GOE, the primary control on seawater sulfate concentration must have been the expansive drawdown of sulfate (as pyrite) into sulfidic environments in the water column and pore waters (Turner and Bekker, 2016). Indeed, there is abundant evidence for euxinic marine conditions in intracratonic basins during the Mesoproterozoic, including the 1.73–1.4 Ga McArthur basin, Australia (Brocks et al., 2005;

636   Shen et al., 2002, 2003), the 1.45 Ga Belt basin (Scott et al., 2008; Lyons et al., 2000), the

637   1.1 Ga Vazante Group, Brazil (Geboy et al., 2013), and the 1.1 Ga Taoudeni Basin,

638   Mauritania (Gilleaudeau and Kah, 2013; Beghin et al., 2017). The predicted low dissolved

639   sulfate concentrations, and the concomitant low-oxygen content of the global ocean, would

640   allow larger hydrothermal and diagenetic fluxes of Fe to spread into the ocean. Coupled with

641   low TOC availability in the BMA sediments (Fig. 4), these conditions likely poised the water

642   column at Fe reduction, rather than sulfate reduction, and thus favoured the development of

643   ferruginous, rather than euxinic, conditions (Poulton and Canfield, 2011).

644   Pyrite sulfur isotope values show more variability in the middle Neoproterozoic Karatau

645   Group (Fig. 4), potentially reflecting an increase in seawater sulfate content due to

646   progressive oxygenation of the atmosphere-ocean system in the run-up to the Cryogenian

647   glaciations (Thomson et al., 2015; Turner and Bekker, 2016). Unfortunately, only a limited

648   number of samples from the Karatau Group yielded enough sulfide for isotopic analysis and

649   hence our data set is too small to warrant a firm interpretation. Nevertheless, in a global study

650   of water column redox conditions, Guilbaud et al. (2015) suggested that seawater sulfate

651   concentrations remained relatively low in the early Neoproterozoic, with the oceanic influx of

652   Fe$_{HR}$ overwhelming the flux of sulfate and thus resulting in a decrease in sulfate availability.

653   This could have resulted in a global expansion of ferruginous conditions, consistent with our

654   data from the BMA.

655   A particularly prominent feature of our data-set is the restriction of oxic water column

656   conditions to the shallowest waters within the Bashkir basin. This is consistent with some

657   inferences based on data from the North China Craton (Luo et al., 2014; Tang et al., 2016),

658   but contrasts with recent evidence for progressive oxygenation and a deepening of the

659   oxycline starting at ~1.57 Ga in the same area (Zhang et al., 2018). In addition, restriction of

660   oxic conditions to very shallow waters contradicts suggestions for a broadly

661   contemporaneous deep water oxygenation event at ~1.4 Ga elsewhere on the North China

662   Craton (Zhang et al., 2016), in the McArthur basin, Northern Australia (Yang et al., 2017), and

663   in the Kama-Belsk aulacogen of the Volga-Ural region of Russia (Sperling et al., 2014).

664   Interestingly, the records of atmosphere-ocean oxygenation in these latter basins are all

665   closely associated with the emplacement of a large igneous province (LIP) linked to the

666   breakup of the Columbia-Nuna supercontinent and the Mashak magmatic event in the BMA

667   at ~1380 Ma (Evans and Mitchell, 2011; Puchkov et al., 2013). It initially seems

668   counterintuitive that atmosphere-ocean oxygenation followed the emplacement of LIPs, since

they should have delivered reductants to the atmosphere and ocean. However, these volcanic outpourings would have also supplied CO_2 and SO_2, which could have enhanced terrestrial chemical weathering, potentially fertilizing the oceans via increased nutrient delivery. Concomitant increases in productivity and organic carbon burial would supply oxidizing equivalents to the Earth system and therefore promote oxygenation. It thus remains to be tested with higher resolution studies whether the spatial and temporal extent of shallow water oxygenation within the Bashkir basin was more variable and dynamic on timescales not encapsulated by our sampling strategy. Nevertheless, our data clearly highlight that in this particular basin, ferruginous conditions dominated in all, but the shallowest environments across a 900-million-year time period.

Considerable uncertainty still remains over the evolution of ocean redox chemistry and levels of atmospheric oxygen through the Mesoproterozoic (Daines et al., 2017; Planavsky et al., 2014; Zhang et al., 2016). Based on a lack of Fe_{HR} and redox-sensitive trace metal enrichments, Sperling et al. (2014) argued for deep water oxygenation at ~1.4 Ga. In many ways, this is a compelling argument, but there are alternative explanations for these data. For example, simple mass balance constraints denote that enrichments in Fe_{HR} are not possible across a globally anoxic ocean. Thus, some areas must constitute a source of Fe_{HR} to allow for enrichments to develop elsewhere (Poulton and Canfield, 2011). In modern anoxic basins, a shallow to deeper basin Fe shuttle is commonly advocated (Anderson and Raiswell, 2004; Severmann et al., 2008). However, modern anoxic basins do not adequately reflect global ocean anoxia, as in ancient settings considerable water column Fe(II) was likely sourced from anoxic non-sulfidic porewaters in the deep ocean (Poulton and Canfield, 2011) as well as from submarine hydrothermal vents (Poulton and Raiswell, 2002). This Fe(II) would upwell onto the continental shelves to sites where water column precipitation was promoted. Thus, under widespread anoxic conditions, deeper sediments *should not* exhibit Fe_{HR} enrichments. In addition, as highlighted in the current study where there is strong evidence for ferruginous conditions, trace metal enrichments in low-TOC, deep water ferruginous settings would not be expected in the absence of an Fe (oxyhydr)oxide shuttle to the sediments (i.e., if the sediments were a source rather than a sink of Fe_{HR}). Consequently, the evidence for deep water oxygenation in the Volga-Ural region remains rather equivocal. Furthermore, based on the Re-Os ages, sediments studied by Sperling et al. (2014) in the Kama-Belsk aulocogen of the Volga-Ural region are correlative to the Middle Riphean Yurmatau Group of the BMA. The Kama-Belsk aulocogen is inland from the continental margin for at least 150 miles,

702 questioning whether these sediments truly record deep water deposition. Similarly, there is
703 considerable debate over the evidence for deeper water oxygenation based on a vanadium
704 depletion at ~1.4 Ga recorded in sedimentary rocks from the North China Craton (Planavsky
705 et al., 2016; Zhang et al., 2016). Multiple redox proxy investigations into the Xiamaling
706 Formation from the North China Craton suggest variable bottom-water chemistry, with
707 evidence for oxic, ferruginous, and even euxinic deposition (Diamond et al., 2018; Wang et
708 al., 2017). These contrasting observations and ongoing debates clearly emphasize the need
709 for further research to evaluate spatial and temporal variability in ocean redox conditions
710 throughout the Mesoproterozoic Era. In the absence of a direct atmospheric proxy, these data
711 will ultimately inform the discussion on the evolution of atmospheric oxygen levels (Daines et
712 al., 2017; Planavsky et al., 2014, 2016; Zhang et al., 2016) over this critical interval in Earth's
713 history.

714

715 **6. Conclusions**

716　Iron speciation analyses provide strong evidence for anoxic water column conditions
717 beneath a very shallow chemocline, throughout deposition of the ~1.75–0.8 Ga sedimentary
718 succession preserved in the Bashkir Meganticlinorium, Southern Urals, Russia. An integrated
719 evaluation of Mo, U, and Mn concentrations provides robust support for this ocean redox
720 reconstruction, and suggests that relatively minor sediment enrichments in Mo resulted from
721 an Fe (oxyhydr)oxide particulate shuttle that operated largely in the absence of dissolved
722 sulfide. Sulfur isotope systematics suggest that ferruginous conditions in the basin likely arose
723 due to low sulfate availability, which was exacerbated by low TOC in an apparently
724 oligotrophic setting. These data add to the growing geochemical database documenting the
725 evolution of ocean redox conditions during the Mesoproterozoic Era. When compared to other
726 studies, the data presented here emphasises the global heterogeneity of water column redox
727 in Mesoproterozoic oceans. This therefore underlines the need for future investigations at a
728 variety of temporal and spatial scales.

729

References

Akimova, G.N. 1967. Cross-bedding in Zil'merdak Formation Rocks in the Southern Urals *In*: *Materialy po stratigrafii i tektonike Urala (Materials on the Stratigraphy and Tectonics of the Urals*. Leningrad: Vses. Geol. Inst., pp. 36–65.

Algeo, T.J. 2004. Can marine anoxic events draw down the trace element inventory of seawater? *Geology*. **32**(12),pp.1057–1060.

Algeo, T.J. and Lyons, T.W. 2006. Mo-total organic carbon covariation in modern anoxic marine environments: Implications for analysis of paleoredox and paleohydrographic conditions. *Paleoceanography*. **21**(1),pp.1–23.

Algeo, T.J. and Tribovillard, N. 2009. Environmental analysis of paleoceanographic systems based on molybdenum-uranium covariation. *Chemical Geology*. **268**(3–4),pp.211–225.

Anderson, R.F., Fleisher, M.Q. and LeHuray, A.P. 1989. Concentration, oxidation state, and particulate flux of uranium in the Black Sea. *Geochimica et Cosmochimica Acta*. **53**(9),pp.2215–2224.

Anderson, T.F. and Raiswell, R. 2004. Sources and mechanisms for the enrichment of highly reactive iron in euxinic Black Sea sediments. *American Journal of Science*. **304**(3),pp.203–233.

Asael, D., Rouxel, O., Poulton, S.W., Lyons, T.W. and Bekker, A. 2018. Molybdenum record from black shales indicates oscillating atmospheric oxygen levels in the early Paleoproterozoic. *American Journal of Science*. **318**(3),pp.275–299.

Bartley, J., Kah, L., Mcwilliams, J. and Stagner, A. 2007. Carbon isotope chemostratigraphy of the Middle Riphean type section (Avzyan Formation, Southern Urals, Russia): Signal recovery in a fold-and-thrust belt. *Chemical Geology*. **237**(1–2),pp.211–232.

Beghin, J., Storme, J.Y., Blanpied, C., Gueneli, N., Brocks, J.J., Poulton, S.W. and Javaux, E.J. 2017. Microfossils from the late Mesoproterozoic – early Neoproterozoic Atar/El Mreïti Group, Taoudeni Basin, Mauritania, northwestern Africa. *Precambrian Research*. **291**(January),pp.63–82.

Bekker, A., Holland, H.D., Wang, P.-L., Rumble, D., Stein, H.J., Hannah, J.L., Coetzee, L.L. and Beukes, N.J. 2004. Dating the rise of atmospheric oxygen. *Nature*. **427**(6970),pp.117–120.

Bellefroid, E.J., Hood, A.v.S., Hoffman, P.F., Thomas, M.D., Reinhard, C.T. and Planavsky, N.J. 2018. Constraints on Paleoproterozoic atmospheric oxygen levels. *Proceedings of the National Academy of Sciences*. **115**(32),pp.8104–8109.

Bertine, K.K. and Turekian, K.K. 1973. Molybdenum in marine deposits. *Geochimica et Cosmochimica Acta*. **37**(6),pp.1415–1434.

Brocks, J.J., Love, G.D., Summons, R.E., Knoll, A.H., Logan, G.A. and Bowden, S.A. 2005. Biomarker evidence for green and purple sulphur bacteria in a stratified Palaeoproterozoic sea. *Nature*. **437**(7060),pp.866–870.

Brumsack, H.J. 2006. The trace metal content of recent organic carbon-rich sediments: Implications for Cretaceous black shale formation. *Palaeogeography, Palaeoclimatology, Palaeoecology*. **232**(2–4),pp.344–361.

Canfield, D.E. 1998. A new model for Proterozoic ocean chemistry. *Nature*. **396**,pp.450–453.

Canfield, D.E. 2000. The Archean Sulfur Cycle and the Early History of Atmospheric Oxygen. *Science*. **288**(5466),pp.658–661.

Canfield, D.E. 2005. The Early History of Atmospheric Oxygen: Homage to Robert M. Garrels. *Annual Review of Earth and Planetary Sciences*. **33**(1),pp.1–36.

Canfield, D.E., Lyons, T.W. and Raiswell, R. 1996. A model for iron deposition to euxinic Black Sea sediments. *American Journal of Science*. **296**(7),pp.818–834.

Canfield, D.E., Raiswell, R., Westrich, J.T., Reaves, C.M. and Berner, R.A. 1986. The use of chromium reduction in the analysis of reduced inorganic sulfur in sediments and shales. *Chemical Geology*. **54**,pp.149–155.

Clarkson, M.O., Poulton, S.W., Guilbaud, R. and Wood, R.A. 2014. Assessing the utility of Fe/Al and Fe-speciation to record water column redox conditions in carbonate-rich sediments. *Chemical Geology*. **382**,pp.111–122.

Cloud, P. 1972. A working model of the primitive Earth. *American Journal of Science*. **272**(6),pp.537–548.

Cole, D.B., Reinhard, C.T., Wang, X., Gueguen, B., Halverson, G.P., Gibson, T., Hodgskiss, M.S.W., Mckenzie, N.R., Lyons, T.W. and Planavsky, N.J. 2016. A shale-hosted Cr isotope record of low atmospheric oxygen during the Proterozoic. *Geology*. (7),pp.1–4.

Cox, G.M., Jarrett, A., Edwards, D., Crockford, P.W., Halverson, G.P., Collins, A.S., Poirier, A. and Li, Z.-X. 2016. Basin redox and primary productivity within the Mesoproterozoic Roper Seaway. *Chemical Geology*. **440**,pp.101–114.

Crockford, P.W., Hayles, J.A., Bao, H., Planavsky, N.J., Bekker, A., Fralick, P.W., Halverson, G.P., Bui, T.H., Peng, Y. and Wing, B.A. 2018. Triple oxygen isotope evidence for limited mid-Proterozoic primary productivity. *Nature*. **559**(7715),pp.613–616.

Cumming, V.M., Poulton, S.W., Rooney, A.D. and Selby, D. 2013. Anoxia in the terrestrial environment during the late Mesoproterozoic. *Geology*. **41**,pp.583–586.

Daines, S.J., Mills, B.J.W. and Lenton, T.M. 2017. Atmospheric oxygen regulation at low Proterozoic levels by incomplete oxidative weathering of sedimentary organic carbon. *Nature Communications*. **8**(Level 7),p.14379.

Diamond, C.W., Planavsky, N.J., Wang, C. and Lyons, T.W. 2018. What the ~1.4 Ga Xiamaling Formation can and cannot tell us about the mid-Proterozoic ocean. *Geobiology*. (October 2017),pp.1–18.

Emerson, S.R. and Huested, S.S. 1991. Ocean anoxia and the concentrations of molybdenum and vanadium in seawater. *Marine Chemistry*. **34**,pp.177–196.

Erickson, B.E. and Helz, G.R. 2000. Molybdenum(VI) speciation in sulfidic waters: Stability and lability of thiomolybdates. *Geochimica et Cosmochimica Acta*. **64**(7),pp.1149–1158.

Ernst, R.E., Pease, V., Puchkov, V.N., Kozlov, V.I., Sergeeva, N.D., Hamilton, M. and Ernst, R.E., Pease, V., Puchkov, V.N., Kozlov, V.I., Sergeeva, N.D., Hamilton, M. 2000. Geochemical Characterization of Precambrian Magmatic Suites of the Southeastern Margin of the East European Craton , Southern Urals , Russia. *Geological collection*. **5**,pp.119–161.

Evans, D.A.D. and Mitchell, R.N. 2011. Assembly and breakup of the core of Paleoproterozoic-Mesoproterozoic supercontinent Nuna. *Geology*. **39**(5),pp.443–446.

Gartman, A. and Luther, G.W. 2014. Oxidation of synthesized sub-micron pyrite (FeS2) in seawater. *Geochimica et Cosmochimica Acta*. **144**,pp.96–108.

Geboy, N.J., Kaufman, A.J., Walker, R.J., Misi, A., de Oliviera, T.F., Miller, K.E., Azmy, K., Kendall, B. and Poulton, S.W. 2013. Re-Os age constraints and new observations of Proterozoic glacial deposits in the Vazante Group, Brazil. *Precambrian Research*.

238,pp.199–213.

Giese, U., Glasmacher, U., Kozlov, V.I., Matenaar, I., Puchkov, V.N., Stroink, L., Bauer, W., Ladage, S. and Walter, R. 1999. Structural framework of the Bashkirian anticlinorium, SW Urals. *Geologische Rundschau*. **87**(4),pp.526–544.

Gilleaudeau, G.J. and Kah, L.C. 2015. Heterogeneous redox conditions and a shallow chemocline in the Mesoproterozoic ocean: Evidence from carbon-sulfur-iron relationships. *Precambrian Research*. **257**,pp.94–108.

Gilleaudeau, G.J. and Kah, L.C. 2013. Oceanic molybdenum drawdown by epeiric sea expansion in the Mesoproterozoic. *Chemical Geology*. **356**,pp.21–37.

Gilleaudeau, G.J.J., Frei, R., Kaufman, A.J.J., Kah, L.C.C., Azmy, K., Bartley, J.K.K., Chernyavskiy, P. and Knoll, A.H.H. 2016. Oxygenation of the mid-Proterozoic atmosphere: clues from chromium isotopes in carbonates. *Geochemical Perspectives Letters*. **2**(2),pp.178–187.

Glasmacher, U.A., Bauer, W., Clauer, N. and Puchkov, V.N. 2004. Neoproterozoic metamorphism and deformation at the southeastern margin of the East European Craton, Uralides, Russia. *International Journal of Earth Sciences*. **93**(5),pp.921–944.

Glasmacher, U.A., Bauer, W., Giese, U., Reynolds, P., Kober, B., Puchkov, V., Stroink, L., Alekseyev, A. and Willner, A.P. 2001. The metamorphic complex of Beloretzk, SW Urals, Russia - A terrane with a polyphase Meso- to Neoproterozoic thermo-dynamic evolution. *Precambrian Research*. **110**(1–4),pp.185–213.

Goldberg, T., Poulton, S.W., Wagner, T., Kolonic, S.F. and Rehkämper, M. 2016. Molybdenum drawdown during Cretaceous Oceanic Anoxic Event 2. *Earth and Planetary Science Letters*. **440**,pp.81–91.

Gorozhanin, V.M., Puchkov, V.N., Gorozhanina, E.N., Sergeeva, N.D., Romanyuk, T.V. and Kuznetsov, N.B. 2014. The Navysh graben-rift of the South Urals as a fragment of the Early Proterozoic aulacogen. *Doklady Earth Sciences*. **458**(1),pp.1052–1057.

Guilbaud, R., Poulton, S.W., Butterfield, N.J., Zhu, M. and Shields-Zhou, G.A. 2015. A global transition to ferruginous conditions in the early Neoproterozoic oceans. *Nature Geoscience*. **8**,pp.466–470.

Gumsley, A.P., Chamberlain, K.R., Bleeker, W., Söderlund, U., de Kock, M.O., Larsson, E.R. and Bekker, A. 2017. Timing and tempo of the Great Oxidation Event.

Proceedings of the National Academy of Sciences. **114**(8),pp.1811–1816.

Habicht, K.S., Gade, M., Thamdrup, B., Berg, P. and Canfield, D.E. 2002. Calibration of Sulfate Levels in the Archean Ocean. *Science*. **298**(5602),pp.2372–2374.

Helz, G.R., Miller, C. V., Charnock, J.M., Mosselmans, J.F.W., Pattrick, R.A.D., Garner, C.D. and Vaughan, D.J. 1996. Mechanism of molybdenum removal from the sea and its concentration in black shales: EXAFS evidence. *Geochimica et Cosmochimica Acta*. **60**(19),pp.3631–3642.

Holland, H.D. 1984. *The chemical evolution of the atmosphere and oceans*. Princeton: Princeton University Press.

Holland, H.D. 2002. Volcanic gases, black smokers, and the Great Oxidation Event. *Geochimica et Cosmochimica Acta*. **66**(21),pp.3811–3826.

Huminicki, D.M.C. and Rimstidt, J.D. 2009. Iron oxyhydroxide coating of pyrite for acid mine drainage control. *Applied Geochemistry*. **24**(9),pp.1626–1634.

Immenhauser, A. 2009. Estimating palaeo-water depth from the physical rock record. *Earth-Science Reviews*. **96**(1–2),pp.107–139.

Kah, L.C., Lyons, T.W. and Frank, T.D. 2004. Low marine sulphate and protracted oxygenation of the Proterozoic biosphere. *Nature*. **431**(October),pp.834–837.

Keller, B.M. and Chumakov, N.M. 1983. *The Riphean Stratotype: Stratigraphy and Geochronology*. Moscow.

Kipp, M.A., Stüeken, E.E., Bekker, A. and Buick, R. 2017. Selenium isotopes record extensive marine suboxia during the Great Oxidation Event. *Proceedings of the National Academy of Sciences*. **114**(5),pp.875–880.

Kipp, M.A., Stüeken, E.E., Yun, M., Bekker, A. and Buick, R. 2018. Pervasive aerobic nitrogen cycling in the surface ocean across the Paleoproterozoic Era. *Earth and Planetary Science Letters*. **500**,pp.117–126.

Klinkhammer, G.P. and Palmer, M.R. 1991. Uranium in the oceans: Where it goes and why. *Geochimica et Cosmochimica Acta*. **55**(7),pp.1799–1806.

Krasnobaev, A.A., Puchkov, V.N., Kozlov, V.I., Sergeeva, N.D., Busharina, S.V and Lepekhina, E.N. 2013. Zirconology of Navysh volcanic rocks of the Ai Suite and the problem of the age of the Lower Riphean boundary in the Southern Urals. *Doklady*

Earth Sciences. **448**(2),pp.185–190.

Kuznetsov, A.B., Bekker, A., Ovchinnikova, G.V., Gorokhov, I.M. and Vasilyeva, I.M. 2017. Unradiogenic strontium and moderate-amplitude carbon isotope variations in early Tonian seawater after the assembly of Rodinia and before the Bitter Springs Excursion. *Precambrian Research*. **298**,pp.157–173.

Kuznetsov, A.B., Ovchinnikova, G. V, Semikhatov, M.A., Gorokhov, I.M., Kaurova, O.K., Krupenin, M.T., Vasil'eva, I.M., Gorokhovskii, B.M. and Maslov, A. V 2008. The Sr isotopic characterization and Pb-Pb age of carbonate rocks from the Satka formation, the Lower Riphean Burzyan Group of the southern Urals. *Stratigraphy and Geological Correlation*. **16**(2),pp.120–137.

Kuznetsov, A.B., Semikhatov, M.A., Gorokhov, I.M., Mel'nikov, N.N., Konstantinova, G.V and Kutyavin, E.P. 2003. Sr isotope composition in carbonates of the Karatau Group, southern Urals, and standard curve of 87Sr/86Sr variations in the Late Riphean Ocean. *Stratigraphy and Geological Correlation*. **11**(5),pp.415–449.

Kuznetsov, A.B., Semikhatov, M.A., Maslov, A. V., Gorokhov, I.M., Prasolov, E.M., Krupenin, M.T. and Kislova, I. V. 2006. New data on Sr-and C-isotopic chemostratigraphy of the Upper Riphean type section (Southern Urals). *Stratigraphy and Geological Correlation*. **14**(6),pp.602–628.

Li, C., Planavsky, N.J., Love, G.D., Reinhard, C.T., Hardisty, D., Feng, L., Bates, S.M., Huang, J., Zhang, Q., Chu, X. and Lyons, T.W. 2015. Marine redox conditions in the middle Proterozoic ocean and isotopic constraints on authigenic carbonate formation: Insights from the Chuanlinggou Formation, Yanshan Basin, North China. *Geochimica et Cosmochimica Acta*. **150**,pp.90–105.

Little, S.H., Vance, D., Lyons, T.W. and McManus, J. 2015. Controls on trace metal authigenic enrichment in reducing sediments: Insights from modern oxygen-deficient settings. *American Journal of Science*. **315**(2),pp.77–119.

Lubnina, N.V., Pisarevsky, S.A., Bogdanova, S.V. and Sokolov, S.J. 2016. Late Paleoproterozoic Paleogeography of Baltica and Laurentia: New Paleomagnetic Data from 1.80–1.75 Ga Mafic Intrusions of Fennoscandia and Sarmatia. *Acta Geologica Sinica*. **90**(July),p.37.

Luo, G., Junium, C.K., Kump, L.R., Huang, J., Li, C., Feng, Q., Shi, X., Bai, X. and Xie, S.

2014. Shallow stratification prevailed for ~1700 to ~1300 Ma ocean: Evidence from organic carbon isotopes in the North China Craton. *Earth and Planetary Science Letters*. **400**,pp.219–232.

Luo, G., Ono, S., Beukes, N.J., Wang, D.T., Xie, S. and Summons, R.E. 2016. Rapid oxygenation of Earths atmosphere 2.33 billion years ago. *Science Advances*. **2**(5),pp.e1600134–e1600134.

Lyons, T.W., Luepke, J.J., Schreiber, M.E. and Zieg, G.A. 2000. Sulfur geochemical constraints on Mesoproterozoic restricted marine deposition: Lower Belt Supergroup, northwestern United States. *Geochimica et Cosmochimica Acta*. **64**(3),pp.427–437.

Lyons, T.W., Reinhard, C.T. and Planavsky, N.J. 2014. The rise of oxygen in Earth's early ocean and atmosphere. *Nature*. **506**(7488),pp.307–315.

Maslov, A.V., Erdtmann, B.-D., Ivanov, K.S., Ivanov, S.N. and Krupenin, M.T. 1997. The main tectonic events, depositional history, and the palaeogeography of the southern Urals during the Riphean-early Palaeozoic. *Tectonophysics*. **276**(1–4),pp.313–335.

Maslov, A.V., Podkovyrov, V.N. and Gareev, E.Z. 2012. Evolution of the paleogeodynamic settings of the formation of the Lower and Middle Riphean sedimentary sequences of the Uchur-Maya region and the Bashkir meganticlinorium. *Russian Journal of Pacific Geology*. **6**(5),pp.382–394.

Maslov, A.V 2002. Facies Associations of Riphean Sedimentary Sequences. *Lithology and Mineral Resources*. **37**(5),pp.462–474.

Maslov, A.V 2004. Riphean and Vendian sedimentary sequences of the Timanides and Uralides, the eastern periphery of the East European Craton. *Geological Society, London, Memoirs*. **30**(1),pp.19–35.

Maslov, A.V., Gareev, E.Z. and Podkovyrov, V.N. 2010. Upper Riphean and Vendian sandstones of the Bashkirian anticlinorium. *Lithology and Mineral Resources*. **45**(September 2015),pp.285–301.

Mukherjee, I. and Large, R.R. 2016. Pyrite trace element chemistry of the Velkerri Formation, Roper Group, McArthur Basin: Evidence for atmospheric oxygenation during the Boring Billion. *Precambrian Research*. **281**,pp.13–26.

Ovchinnikova, G.V., Kuznetsov, A.B., Vasil'eva, I.M., Gorokhov, I.M., Krupenin, M.T., Gorokhovskii, B.M. and Maslov, A.V. 2013. Pb-Pb age and Sr isotopic characteristic of

the Middle Riphean phosphorite concretions: The Zigaza-Komarovo Formation of the South Urals. *Doklady Earth Sciences*. **451**(4),pp.798–802.

Partin, C.A., Bekker, A., Planavsky, N.J., Scott, C.T., Gill, B.C., Li, C., Podkovyrov, V., Maslov, A., Konhauser, K.O., Lalonde, S.V., Love, G.D., Poulton, S.W. and Lyons, T.W. 2013. Large-scale fluctuations in Precambrian atmospheric and oceanic oxygen levels from the record of U in shales. *Earth and Planetary Science Letters*. **369–370**,pp.284–293.

Planavsky, N.J., Cole, D.B., Reinhard, C.T., Diamond, C., Love, G.D., Luo, G., Zhang, S., Konhauser, K.O. and Lyons, T.W. 2016. No evidence for high atmospheric oxygen levels 1,400 million years ago. *Proceedings of the National Academy of Sciences*. **113**(19),pp.E2550–E2551.

Planavsky, N.J., McGoldrick, P., Scott, C.T., Li, C., Reinhard, C.T., Kelly, A.E., Chu, X., Bekker, A., Love, G.D. and Lyons, T.W. 2011. Widespread iron-rich conditions in the mid-Proterozoic ocean. *Nature*. **477**(7365),pp.448–451.

Planavsky, N.J., Reinhard, C.T., Wang, X., Thomson, D., Mcgoldrick, P., Rainbird, R.H., Johnson, T.M., Fischer, W.W. and Lyons, T.W. 2014. Low Mid-Proterozoic atmospheric oxygen levels and the delayed rise of Animals. *Science*. **346**(6209),pp.635–638.

Planavsky, N.J., Slack, J.F., Cannon, W.F., O'Connell, B., Isson, T.T., Asael, D., Jackson, J.C., Hardisty, D.S., Lyons, T.W. and Bekker, A. 2018. Evidence for episodic oxygenation in a weakly redox-buffered deep mid-Proterozoic ocean. *Chemical Geology*. **483**,pp.581–594.

Poulton, S.W. and Canfield, D.E. 2005. Development of a sequential extraction procedure for iron: implications for iron partitioning in continentally derived particulates. *Chemical Geology*. **214**(3–4),pp.209–221.

Poulton, S.W. and Canfield, D.E. 2011. Ferruginous Conditions: A Dominant Feature of the Ocean through Earth's History. *Elements*. **7**(2),pp.107–112.

Poulton, S.W., Fralick, P.W. and Canfield, D.E. 2010. Spatial variability in oceanic redox structure 1.8 billion years ago. *Nature Geoscience*. **3**(7),pp.486–490.

Poulton, S.W., Fralick, P.W. and Canfield, D.E. 2004. The transition to a sulphidic ocean ~1.84 billion years ago. *Nature*. **431**(September),pp.173–177.

Poulton, S.W. and Raiswell, R. 2002. The low-temperature geochemical cycle of iron: From

continental fluxes to marine sediment deposition. *American Journal of Science*. **302**(9),pp.774–805.

Puchkov, V.N. 1997. Structure and geodynamics of the Uralian orogen. *Geological Society, London, Special Publications*. **121**(121),pp.201–236.

Puchkov, V.N., Bogdanova, S. V., Ernst, R.E., Kozlov, V.I., Krasnobaev, A.A., Söderlund, U., Wingate, M.T.D., Postnikov, A. V. and Sergeeva, N.D. 2013. The ca. 1380Ma Mashak igneous event of the Southern Urals. *Lithos*. **174**,pp.109–124.

Raiswell, R. and Canfield, D.E. 1996. Rates of reaction between silicate iron and dissolved sulfide in Peru Margin sediments. *Geochimica et Cosmochimica Acta*. **60**(15),pp.2777–2787.

Raiswell, R. and Canfield, D.E. 1998. Sources of iron for pyrite formation in marine sediments. *American Journal of Science*. **298**(3),pp.219–245.

Raiswell, R. and Canfield, D.E. 2012. The Iron Biogeochemical Cycle Past and Present. *Geochemical Perspectives*. **1**(1),pp.1–220.

Raiswell, R., Canfield, D.E. and Berner, R.A. 1994. A comparison of iron extraction methods for the determination of degree of pyritisation and the recognition of iron-limited pyrite formation. *Chemical Geology*. **111**,pp.101–110.

Raiswell, R., Newton, R., Bottrell, S.H., Coburn, P.M., Briggs, D.E.G., Bond, D.P.G. and Poulton, S.W. 2008. Turbidite depositional influences on the diagenesis of Beecher's Trilobite Bed and the Hunsrück Slate; sites of soft tissue pyritization. *American Journal of Science*. **308**(2),pp.105–129.

Raiswell, R., Newton, R. and Wignall, P.B. 2001. An Indicator of Water-Column Anoxia: Resolution of Biofacies Variations in the Kimmeridge Clay (Upper Jurassic, U.K.). *Journal of Sedimentary Research*. **71**(2),pp.286–294.

Reinhard, C.T., Planavsky, N.J., Robbins, L.J., Partin, C.A., Gill, B.C., Lalonde, S. V, Bekker, A., Konhauser, K.O. and Lyons, T.W. 2013. Proterozoic ocean redox and biogeochemical stasis. *Proceedings of the National Academy of Sciences of the United States of America*. **110**,pp.5357–62.

Romanyuk, T.V., Maslov, A.V., Kuznetsov, N.B., Belousova, E.A., Ronkin, Y.L., Krupenin, M.T., Gorozhanin, V.M., Gorozhanina, E.N. and Seregina, E.S. 2013. First data on LA-ICP-MS U/Pb zircon geochronology of Upper Riphean sandstones of the Bashkir

Anticlinorium (South Urals). *Doklady Earth Sciences*. **452**(2),pp.997–1000.

Ronkin, Y.L., Maslov, A.V, Kazak, A.P., Matukov, D.I. and Lepikhina, O.P. 2007. The Lower-Middle Riphean boundary in the southern Urals: new isotopic U-Pb (SHRIMP II) constraints. *Doklady Earth Sciences*. **415**(2),pp.835–840.

Scholz, F., McManus, J. and Sommer, S. 2013. The manganese and iron shuttle in a modern euxinic basin and implications for molybdenum cycling at euxinic ocean margins. *Chemical Geology*. **355**,pp.56–68.

Scott, C., Lyons, T.W., Bekker, A., Shen, Y., Poulton, S.W., Chu, X. and Anbar, A.D. 2008. Tracing the stepwise oxygenation of the Proterozoic ocean. *Nature*. **452**(7186),pp.456–9.

Semikhatov, M.A., Kuznetsov, A.B. and Chumakov, N.M. 2015. Isotope age of boundaries between the general stratigraphic subdivisions of the Upper Proterozoic (Riphean and Vendian) in Russia: The evolution of opinions and the current estimate. *Stratigraphy and Geological Correlation*. **23**(6),pp.568–579.

Semikhatov, M.A., Kuznetsov, A.B., Maslov, A.V, Gorokhov, I.M. and Ovchinnikova, G.V 2009. Stratotype of the Lower Riphean, the Burzyan Group of the Southern Urals: Lithostratigraphy, paleontology, geochronology, Sr- and C-isotopic characteristics of its carbonate rocks. *Stratigraphy and Geological Correlation*. **17**(6),pp.574–601.

Severmann, S., Lyons, T.W., Anbar, A., McManus, J. and Gordon, G. 2008. Modern iron isotope perspective on the benthic iron shuttle and the redox evolution of ancient oceans. *Geology*. **36**(6),pp.487–490.

Shatsky, N.S. 1945. *Sketches on the tectonics of the Volga-Urals oil region and the adjacent part of the western slope of the South Urals*. Moscow.

Shatsky, N.V. 1960. Principles of stratigraphy of the Late Precambrian and volume of the Riphean Group *In*: *Stratigraphy of the Late Precambrian and Cambrian (IGC, XXI Session, Problem 8), AN SSSR*. Moscow.

Shen, Y., Canfield, D.E. and Knoll, A.H. 2002. Middle Proterozoic Ocean Chemistry: Evidence from the McArthur Basin, Northern Australia. *American Journal of Science*. **302**(February),pp.81–109.

Shen, Y., Knoll, A.H. and Walter, M.R. 2003. Evidence for low sulphate and anoxia in a mid-Proterozoic marine basin. *Nature*. **423**(June),pp.632–635.

Slack, J.F. and Cannon, W.F. 2009. Extraterrestrial demise of banded iron formations 1.85 billion years ago. *Geology*. **37**(11),pp.1011–1014.

Slack, J.F., Grenne, T., Bekker, A., Rouxel, O.J. and Lindberg, P.A. 2007. Suboxic deep seawater in the late Paleoproterozoic: Evidence from hematitic chert and iron formation related to seafloor-hydrothermal sulfide deposits, central Arizona, USA. *Earth and Planetary Science Letters*. **255**(1–2),pp.243–256.

Sperling, E.A., Rooney, A.D., Hays, L., Sergeev, V.N., Vorob'eva, N.G., Sergeeva, N.D., Selby, D., Johnston, D.T. and Knoll, A.H. 2014. Redox heterogeneity of subsurface waters in the Mesoproterozoic ocean. *Geobiology*. **12**(5),pp.373–86.

Tang, D., Shi, X., Wang, X. and Jiang, G. 2016. Extremely low oxygen concentration in mid-Proterozoic shallow seawaters. *Precambrian Research*. **276**,pp.145–157.

Thomson, D., Rainbird, R.H., Planavsky, N., Lyons, T.W. and Bekker, A. 2015. Chemostratigraphy of the Shaler Supergroup, Victoria Island, NW Canada: A record of ocean composition prior to the Cryogenian glaciations. *Precambrian Research*. **263**,pp.232–245.

Tosca, N.J., Guggenheim, S. and Pufahl, P.K. 2016. An authigenic origin for Precambrian greenalite: Implications for iron formation and the chemistry of ancient seawater. *Bulletin of the Geological Society of America*. **128**(3–4),pp.511–530.

Tribovillard, N., Algeo, T.J., Baudin, F. and Riboulleau, A. 2012. Analysis of marine environmental conditions based on molybdenum-uranium covariation-Applications to Mesozoic paleoceanography. *Chemical Geology*. **324**–**325**,pp.46–58.

Turekian, K.K. and Wedepohl, K.H. 1961. Distribution of the Elements in Some Major Units of the Earth's Crust. *Geological Society of America Bulletin*. **22**(February),pp.175–192.

Turner, E.C. and Bekker, A. 2016. Thick sulfate evaporite accumulations marking a mid-neoproterozoic oxygenation event (Ten Stone Formation, Northwest territories, Canada). *Bulletin of the Geological Society of America*. **128**(1–2),pp.203–222.

Wang, W., Guan, C., Zhou, C., Peng, Y., Pratt, L.M., Chen, X., Chen, L., Chen, Z., Yuan, X. and Xiao, S. 2017. Integrated carbon, sulfur, and nitrogen isotope chemostratigraphy of the Ediacaran Lantian Formation in South China: Spatial gradient, ocean redox oscillation, and fossil distribution. *Geobiology*. **15**(4),pp.552–571.

Williamson, M.A. and Rimstidt, J.D. 1994. The kinetics and electrochemical rate-determining

step of aqueous pyrite oxidation. *Geochimica et Cosmochimica Acta*. **58**(24),pp.5443–5454.

Yang, H., Chen, Z. and Fang, Y. 2017. Microbially induced sedimentary structures from the 1.64 Ga. *Palaeogeography, Palaeoclimatology, Palaeoecology*. **474**,pp.7–25.

Yang, S., Kendall, B., Lu, X., Zhang, F. and Zheng, W. 2017. Uranium isotope compositions of mid-Proterozoic black shales: Evidence for an episode of increased ocean oxygenation at 1.36 Ga and evaluation of the effect of post-depositional hydrothermal fluid flow. *Precambrian Research*. **298**,pp.187–201.

Zhang, K., Zhu, X., Wood, R.A., Shi, Y., Gao, Z. and Poulton, S.W. 2018. Oxygenation of the Mesoproterozoic ocean and the evolution of complex eukaryotes. *Nature Geoscience*. **11**(5),pp.345–350.

Zhang, S., Wang, X., Wang, H., Bjerrum, C.J., Hammarlund, E.U., Costa, M.M., Connelly, J.N., Zhang, B., Su, J. and Canfield, D.E. 2016. Sufficient oxygen for animal respiration 1,400 million years ago. *Proceedings of the National Academy of Sciences*. **113**(7),pp.1731–1736.